POLITECNICO
MILANO 1863

SCUOLA DI INGEGNERIA INDUSTRIALE
E DELL'INFORMAZIONE

Mathematical modelling and parameter classification for symmetric- and full-cell batteries with metallic anodes

Tesi di Laurea Magistrale in
ENERGY ENGINEERING- INGEGNERIA ENERGETICA

Chiara Marino, 259482

Advisor:
Prof. Benedetto Bozzini

Co-advisors:
Dott.ssa Elisa Emanuele
Prof.ssa Ivonne Sgura

Academic year:
2025-2026

Abstract:
Galvanostatic cycling of symmetric metal cells provides a fundamental platform for investigating morphological instabilities in high-energy-density batteries. However, conventional analysis of Zn/Zn symmetric cells typically relies on integral descriptors such as time-to-failure, neglecting the rich physico-chemical information encoded in voltage transients. This work introduces a physics-based framework combining the Metal Anode Charging (MAC) model with automated waveform classification. Voltage transients are rigorously categorized into four characteristic morphological families based on curvature and derivative signatures, each corresponding to distinct regimes of ion transport, kinetics, dendritic growth, and passivation. A MATLAB-based recognition algorithm enables high-throughput analysis of experimental datasets, revealing how additives and electrode fabrication methods modulate morphological evolution and degradation pathways. The framework is further extended from symmetric Zn/Zn cells to a full Ni/Zn configuration by incorporating a thermodynamically consistent description of the Ni/NiOOH cathode based on the two-parameter Margules formalism. This transition converts the system from a transport-dominated symmetric problem into an asymmetric hybrid model coupling morphology-controlled zinc growth with solid-state intercalation thermodynamics. The results demonstrate that voltage waveform morphology constitutes a robust diagnostic descriptor linking electrochemical signatures to underlying physical regimes. By shifting the focus from parameter fitting to morphology-based interpretation, this approach establishes a generalizable methodology for physically informed monitoring of zinc-based energy storage systems.

Key-words: zinc metal anode; voltage transient; shape classification; MAC model; Ni–Zn full cell; morphology

1. Introduction

The global transition toward sustainable energy systems and the increasing electrification of mobility have significantly intensified the demand for safe, reliable, and cost-effective electrical energy storage technologies [1, 2]. In this scenario, aqueous zinc-based batteries have emerged as a primary candidate for large-scale applications due to the high theoretical capacity of zinc metal, its low cost, global abundance, and the intrinsic safety provided by non-flammable aqueous electrolytes [3, 4] [5]. However, the practical deployment of these

systems remains hindered by the morphological instability of the zinc anode during cycling, specifically the uncontrollable growth of dendrites and the occurrence of surface passivation [6–9]: These phenomena lead to internal short circuits and capacity fade, which represent the principal failure modes for next-generation zinc batteries [1–3, 7].

Despite the large amount of experimental data generated through galvanostatic cycling [8, 10, 11], often using symmetric Zn/Zn cells to isolate anodic and cathodic processes, traditional analysis is typically restricted to integral descriptors, such as time-to-failure [1, 1, 2, 11]. This approach neglects the rich reservoir of physico-chemical information embedded within the voltage–time transients [12–14]. Consequently, a significant methodological gap exists between materials science and device engineering, necessitating the development of theoretical tools capable of quantitatively linking macroscopic electrical signatures to the internal evolution of cell materials [2, 15–18].

To address this challenge, the Metal Anode Charging (MAC) framework was developed [1, 2, 10]. This model, based on a system of coupled partial differential equations (PDEs)[19], describes ion transport, electrochemical kinetics, and the dynamic evolution of electrode shape [1]. Unlike earlier models that assumed a perfectly reversible planar regeneration of the electrode [8, 9], the MAC framework explicitly accounts for irreversibility in both the cathodic (deposition) and anodic (stripping) half-cycles, capturing the cumulative effects of dendritic growth and passivation [1, 2].

The present work provides a comprehensive diagnostic framework for both symmetric and full-cell configurations by linking macroscopic electrical transients to internal electrode dynamics. In the first part of this study, we focus on symmetric Zn/Zn cells, where voltage transients are systematically classified into four fundamental morphological families: single-minimum, extremum-reversal, monotonically increasing, and monotonically decreasing [12]. To facilitate high-throughput analysis, a custom MATLAB-based algorithm was developed to automatically recognize these characteristic shapes in experimental datasets. This algorithm processes individual semi-periods by dividing the signal into six equal sub-intervals and applying rule-based logic to the sign patterns of the mean derivatives, effectively moving beyond simple lifetime metrics toward a morphology-aware diagnostic approach [12]. This recognition framework is applied to evaluate the impact of additives [9, 20–22]from the NDSB series and the influence of fabrication techniques, such as mechanical punching and laser cutting, and other operating condition, on the stability of the metallic deposit.

Furthermore, in this thesis work, I am extending the MAC model beyond the symmetric cell case of interest only for material RD work to the general full-cell case, able to account for practical batteries with a metal anode and an intercalation cathode. Specifically, but without loss of generality, we considered Ni cathodes, but any cathodic chemistry can be accommodated in this model by simple parameter selection, based on standard electrochemical tests. To achieve this, a new governing equation for the nickel hydroxide cathode was developed, providing a thermodynamically consistent description based on the two-parameter Margules formalism established in classical thermodynamic analyses of the nickel electrode [23, 24], but extending it to the out of equilibrium case with interpolating functions for the model parameters. This formulation moves beyond ideal mixture model, expressing the reversible potential as an analytical function of the mole fraction of the reduced species, incorporating an excess Gibbs free energy term derived from Wohl's expansion [23, 24]. The resulting equation combines the standard potential and logarithmic ideal mixing with a quadratic correction that accounts for non ideal interactions and ordered proton insertion into the host lattice [23].

By integrating these solid-state intercalation model directly into the boundary conditions at the nickel electrode interface, while the zinc electrode remains governed by morphology-driven transport and kinetics, the system evolves from a transport-dominated symmetric problem into an asymmetric hybrid framework [2, 23]. Following this theoretical extension, the automated shape-recognition algorithm was adapted for the full-cell configuration. This updated recognition framework is designed to handle variable-duration semi-periods determined by voltage cut-offs and to account for the unique electrical signatures of solid-state intercalation electrodes, enabling high-throughput identification of degradation pathways in practical nickel-zinc energy storage systems.

Finally, while this study focuses on physics-based modelling and qualitative classification, it is important to note that parallel advancements have demonstrated the efficacy of Deep Learning techniques, such as hybrid CNN-LSTM neural networks [11], and K-Means clustering based on Sobolev distances [12] for the automatic identification of physical parameters and shape recognition. By establishing a cogent link between electrical operando data and material dynamics, this unified approach provides a powerful tool for the optimization and diagnostic monitoring of next-generation zinc-based energy storage systems [2, 3].

2. Modeling Framework

2.1. Overview of the MAC model for a symmetric cell

The MAC model [2, 19] is a mathematical framework based on partial differential equations developed to describe the response of symmetric electrochemical cells with metallic electrodes, such as Zn/Zn and Li/Li systems, when subjected to square-wave current inputs. Its primary objective is to link the measured electrical response (cell voltage transient) with the electrode shape evolution occurring during the discharge and the charge of the cell, due to mass transport phenomena, electrochemical kinetics, morphology passivation evolution and the metal anode shape [25–27].
The model accounts for two major irreversible mechanism: dendrite formation and passivation.
Dendrites are metallic structures that grow uncontrollably on the electrode surface, driven by localized high current densities, and can ultimately lead to battery failure. To describe these phenomena the model, consider two assumption: geometric assumption: deposit or dissolved metal is assumed to form hemispherical protrusions arranged on a flat surface in a square lattice with a radius equal to rmax, and to capture morphological instabilities, it has been assumed that during the cathodic cycle (electrodeposition) new metal forms exclusively on the hemispherical protrusion and not on the flat surfaces, while during the anodic cycle the metal dissolve from both the hemispherical and the flat [28].
Passivation inside the model [2], is treated as a kinetic irreversibility and it is included inside the BC. Physically it represents the progressive loss of area due to the ZnO and other species' precipitation on the electrode surface, decreasing the active site surface fraction; its reduce the apparent exchange kinetics increasing the overpotential at fixed current.

2.2. Governing equation

The mathematical framework of the MAC model is established within a one-dimensional electrolyte domain defined as $0 \leq x \leq L$. The system is characterized by two fundamental state variables: the metal-ion concentration $u(x,t)$, and the electrolyte potential $\phi(x,t)$. The governing equations consist of a mass balance for metal ions:
The governing equations consist of a mass balance for metal ions:

$$\frac{\partial u}{\partial t} = -\frac{\partial J}{\partial x} \tag{1}$$

and Laplace's equation for the electric potential distribution:

$$\frac{\partial^2 \phi}{\partial x^2} = 0 \tag{2}$$

The ionic flux J is defined by both diffusion and migration components as

$$J = -D\frac{\partial u}{\partial x} - \frac{zDF}{RT}\, u\, \frac{\partial \phi}{\partial x} \tag{3}$$

At the boundaries x=0 and x=L, the surface potential and ion concentration are coupled through Nernst relations:

$$\phi(x,t) = \frac{RT}{zF} \ln\left(\frac{u(x,t)}{u_0}\right) \tag{4}$$

Additionally, the ionic flux at these boundaries must matches the applied current density i(t);

$$-D\frac{\partial u}{\partial x}\Big|_{x=0,t} - \frac{zDF}{RT}\, u(x=0,t)\frac{\partial \phi}{\partial x}\Big|_{x=0,t} = i(t)\, zF \tag{5}$$

$$-D\frac{\partial u}{\partial x}\Big|_{x=L,t} - \frac{zDF}{RT}\, u(x=L,t)\frac{\partial \phi}{\partial x}\Big|_{x=L,t} = i(t)\, zF \tag{6}$$

Where the ionic flux is expressed as function of the concentrations' and potential's gradient.
The current density i(t), is corrected to reflect the evolving active electrode area; this correction follows the relation:

$$i(t) = \frac{I(t)}{\left[A\frac{K_0(t)}{K_{0,hs}}\right]} \tag{7}$$

where $K_0(t)$ is a time-dependent parameter that accounts for surface growth and passivation. Specifically, this parameter increases with the development of the electrode surface and decreases as passivation occurs. Finally, the measured cell voltage is computed by aggregating the electrolyte potential drop $\Delta\phi$, the ohmic drop term $\Delta\phi = |\phi_L - \phi_0|$, and the cathodic and anodic overpotentials η_{cat} and η_{an}. These activation overpotentials are expressed in a Tafel-type form to provide a comprehensive analytical expression for the voltage transient (eq.23):

$$\Delta\Phi = \Delta\phi + \frac{A}{k}Li + 2B\ln\left[0.5\left(\frac{i}{i_0} + \sqrt{\left(\frac{i}{i_0}\right)^2 + 4}\right)\right] \tag{8}$$

Ko(t) expression is obtained starting from the radius of the hemisphere (we have assumed that the deposit or dissolved metal rearrange on the surface with a perfect hemispherical shape):

$$r(t) = \left(\frac{3IT}{4\pi zF\rho}\Lambda(t;T)\right)^{\frac{1}{3}} \tag{9}$$

From this expression we can derive the fraction of hemispherical and flat portion, of the surface area:

$$\vartheta_{hs}(t) = \frac{A_{hs}(t)}{A_{hs}(t) + A_{rf}(t)} = \frac{2\pi r(t)^2}{4r(t)^2 + \pi r(t)^2} \tag{10}$$

$$\vartheta_{flat}(t) = 1 - \vartheta_{hs}(t) \quad (t \le t_{max}) \tag{11}$$

The model also considers the passivation effect by introducing two degrees of passivation (passivation rate):

$$\vartheta_{hs,pass}(t) = \int_0^{t_{anod}(t)} k_{hs,pass}\,\vartheta_{hs}(\tau)\,d\tau \tag{12}$$

$$\vartheta_{flat,pass}(t) = \int_0^{t_{anod}(t)} k_{flat,pass}\,\vartheta_{flat}(\tau)\,d\tau \tag{13}$$

where $k_{hs,pass}$ and $k_{flat,pass}$ are passivation rate, which represent how fast those surfaces (flat or hemispherical) become passivate, so inactive due to precipitation of different species like ZnO. Like many others parameters, they are strictly related to the materials proprieties, and they must been identify sperimentally. The two constants have different value since passivation is strongly influenced by the gravity, so the electrode which face up, has much higher passivation rate.
It has been also introduced two different effective kinetics, empiric, constant to quantify the electrodeposition and stripping process by expressive how 'reactive' is a certain surface: k0,hs represent the kinetics on top of the hemispherical protuberance, and mostly depends on the tip current on the top of the metal structure; k0,flat instead, refers to the kinetics on the flat portion of the electrodes where no metal growth is occurring. Those two parameters are variable parameters since depend on the material's propriety and on the electrolyte's condition (type of additives).
The final expression of Ko(t) can be now obtained by putting together all those parameters:

$$k_0(t) = k_{0,hs}\,\vartheta_{hs}(t)\,[1 - \vartheta_{hs,pass}(t)] + k_{0,flat}\,\vartheta_{flat}(t)\,[1 - \vartheta_{flat,pass}(t)] \tag{14}$$

2.3. PDE solution

The solution procedure for the MAC model [2, 19] follows a structured numerical approach to correlate internal physical changes with the external electrical response. The process begins with problem initialization, where all model parameters, including operating conditions such as current density and cycle period, are defined alongside constant material properties like molar density and valence. Initial conditions are assigned by setting a uniform metal-ion concentration u_0 across the 1D domain and establishing the initial electrolyte potential distribution. Before solving the core transport equations at each time step, the model performs a pre-PDE update of the effective kinetic parameter K_0. This step evaluates the current state of electrode outgrowth and the accumulated level of passivation, which physically represents the precipitation of species like ZnO on the electrode surface. These morphological and chemical effects are integrated into the kinetic parameter without modifying the physical 1D spatial domain or the electrode geometry itself; instead, they are accounted for through their electrochemical impact on the boundary conditions, specifically by correcting the effective current density.
The PDE solution phase involves the simultaneous calculation of the electrolyte potential $\phi(x,t)$, and the ion concentration u(x,t) for each time step. The potential is determined by solving the Laplace equation, while

the concentration is governed by the mass balance equation, which accounts for both diffusion and migration. These two variables are coupled at the boundaries through Nernst relations, ensuring that the surface potential remains consistent with the local ion concentration at the electrode-electrolyte interface. This system is typically integrated using numerical solvers like MATLAB's PDEPE or custom finite difference schemes that handle the non-homogeneous boundary conditions.
Finally, the model undergoes post-processing to determine the measured cell voltage. The total voltage transient is obtained by summing the electrolyte potential drop between the electrodes, the ohmic contribution associated with the cell's resistance, and the activation overpotentials for both anodic and cathodic charge transfer, which are expressed in a Tafel-type form. This final step allows for the direct comparison of the model's output with experimental galvanostatic cycling data.

3. EXTENSION OF THE MAC MODEL FOR A FULL CELL

The selection of a Nickel-zinc (Ni-Zn) configuration for this study is driven by the many advantages offered by combining a nickel-based cathode with a zinc anode. The nickel hydroxide cathode is a well-established technology known for its high power density, reliability, and excellent discharge rate capabilities [29–33]. When paired with a zinc electrode, the resulting system provides a higher cell voltage (approximately 1.73 V) compared to traditional aqueous systems like Nickel-Cadmium (Ni-Cd) (approximately 1.2 V) [29], or Nickel-Metal Hydride (Ni-MH) (approximately 1.2 V) [29]. Furthermore, zinc is an ideal active material due to its low cost, global abundance, and low toxicity, making it a sustainable alternative to more expensive or environmentally harmful metals [34–38] .From a performance perspective, the high theoretical capacity of zinc, coupled with the stability of the nickel cathode in aqueous electrolytes, creates a battery chemistry that is inherently safe, non-flammable, and capable of delivering significant energy density for various applications [39–41].

3.1. Ni/NiOOH cathode introduction

Positive electrodes for use in NiMH batteries, whether cylindrical or prismatic, can be of the sintered or pasted type, which are also common to NiCd batteries. The nickel hydroxide for use in NiMH batteries is fundamentally the same as that used in NiCd and NiFe, and from a simple viewpoint, the basic compound is the same as that used by Edison and Junger 100 years ago. However, today's high-performance nickel hydroxide is more advanced and continues to improve in capacity, utilization, power and discharge rate capability, cycle life, high temperature charging efficiency, and cost [42–44].
Spherical Nickel Hydroxide. As mentioned previously, one type of nickel hydroxide is by far the most common—a high-density spherical type used in pasted electrodes which became commercial around 1990. High-density spherical nickel hydroxide is made in a precipitation reactor where metal salts such as nickel sulfate are reacted with a caustic such as NaOH in the presence of ammonia [29, 44]. The nickel source may have additives such as cobalt and zinc to enhance performance [29, 30, 44]. The important physical parameters within this type of nickel hydroxide are:
• Chemical formula: The nickel hydroxide active material itself is most commonly a NiCoZn tri-precipitate; a common composition is Ni94Co3Zn3 [29, 44]. However, the amounts of cobalt and zinc, which are usually about 1 to 5
• Tap density: Usually around 2.2 g/cc, tap density is a measure of the dry nickel hydroxide powder packing efficiency and influences the amount of active material that can be loaded into the pores of the nickel foam current collector [29, 44].
• Particle size: An average particle size of about 10 microns [29, 44].
• Surface area: Measured by the BET method, surface area refers not to the geometric area of each nickel hydroxide sphere, but rather to the total surface area of each particle, which contributes to the charge-discharge reactions and can thus affect utilization and high-rate discharge capability. Typical BET surface area for high-density spherical nickel hydroxide is about 10 to 20 m2/g [34, 44]..
• Crystallinity: Each nickel hydroxide sphere has an extremely high surface area corresponding to the nickel hydroxide crystallites themselves [42, 43]. Crystallinity is measured by X-ray diffraction, where the full width at half maximum (FWHM) of a reflection, such as the <101> plane, may yield a typical crystallite size of about 110 Å. A variety of other factors contribute to performance, such as impurities from processing like residual, such as: sulfates, nitrates and sodium sulfate, among others [44]. The more common pasted nickel hydroxide positive electrode is typically produced by mechanically pasting high-density spherical nickel hydroxide into the pores of a foam metal substrate [29, 44]. The foam metal substrate is typically produced by coating polyurethane foam with a layer of nickel by electroplating or by chemical vapor deposition, followed by a heat treatment process to remove the base polyurethane. The foam is then physically loaded with nickel hydroxide having an average diameter of about 10 microns in a paste containing conductive cobalt oxides, which form a conductive network

to compensate for the large distance from the nickel hydroxide to the metal current collector and for the fact that the nickel hydroxide itself is relatively low in conductivity. Usually, the paste additives are finely divided cobalt metal and cobalt monoxide that will dissolve and reprecipitate on the surface of the nickel hydroxide active material. However, the coating may not be uniform and complete in coverage. For ultra-high-power discharge, it is possible to add metallic nickel fibers to the paste formula to enhance conductivity [29, 44]. In the case of calcium additives, the additive may cause a loss in power and/or cycle life. Cobalt metal and cobalt monoxide are relatively expensive battery materials, and increased use has cost implications[45]. Addition of metallic nickel fibers lowers the amount of active material, resulting in reduced capacity and specific energy
During discharge, nickel oxyhydroxide is reduced to nickel hydroxide

$$\mathrm{NiOOH + H_2O + e^- \rightarrow Ni(OH)_2 + OH^-} \qquad E^\circ = 0.52\,\mathrm{V} \tag{15}$$

The process is reversed during charge. N/P ratios vary by cell design and for a given manufacturer but are typically within the range of 1.3 to 2.0. The lower N/P values are used to maximize energy while higher values are used in power and cycle life designs [29, 44].The useful capacity of the battery is thus determined by the positive electrode. A convenient method to fully charge sealed NiMH batteries is to charge at a constant current at about 0.1 C. rate with time limited charge termination. The charge should be terminated after 150
Ni Cathode in Ni-Zn battery: The positive electrode is very similar to that used in nickel-metal hydride and nickel-cadmium systems. The chemistry of the nickel-zinc battery system is similar to that of nickel-cadmium, except that cadmium is replaced by zinc. The electrolyte is typically a 3 to 8 M alkali metal hydroxide solution in which specific additives are sometimes added to improve the charge–discharge behaviour of the zinc electrode [29, 31–33]. The active material of the positive electrode is nickel (III) oxy-hydroxide and that for the negative electrode is high surface area metallic zinc. When discharged, the nickel(III) oxy-hydroxide is reduced to nickel (II) hydroxide and zinc is oxidized to zinc (II) species. The electrochemistry and mechanism of the reactions are quite complex and for illustrative purposes, the simplified forms of the reactions are given below [31, 33].Depending on the conditions, zinc hydroxide, zincate, or zinc oxide and their mixtures may constitute the final reaction product at the negative electrode on discharge. All may be reconverted to zinc during the charging process.

$$\mathrm{Zn + 2OH^- \rightarrow Zn(OH)_2 + 2e^-} \qquad E^\circ = -1.24\,\mathrm{V}$$

$$\mathrm{Zn(OH)_2 + 2OH^- \rightarrow ZnO_2^{2-} + 2H_2O}$$

$$\mathrm{ZnO_2^{2-} + H_2O \rightarrow ZnO + 2OH^-}$$

Positive electrode discharge reactions:

$$\mathrm{2NiOOH + 2H_2O + 2e^- \rightarrow 2Ni(OH)_2 + 2OH^-} \qquad E^\circ = 0.49\,\mathrm{V}$$

3.2. Modelling of Ni/NiOOH cathode charge-discharge curves

Voltage vs. Depth of Discharge (DoD) curves, measured as detailed in Section 3.2.3, were modelled with the two-parameter Margules (TPM) model [23]. This literature model was found to accurately capture the non-idealities in the three key electrode conditions: (i) at equilibrium; (ii) as a function of the discharge/charge current and (iii) as a function of degradation degree.
The two-parameter Margules model is a thermodynamic framework, based on binary solution theory, employed to describe the reversible potential of the nickel hydroxide electrode as a function of its state-of-discharge, specifically accounting for non-idealities in the mixing of solid species. Unlike simpler models, it moves beyond the assumption of ideal behavior or random insertion, offering a more sophisticated representation of the complex interactions within the active material, as detailed below.

3.2.1 Model formulation

The foundation of this model lies in the Gibbs free energy of mixing ΔG_{mix} which, for non-ideal systems, is expressed as the sum of three components [24]:

- Free energy due to ideal mixing, ΔG_{id};
- Free energy due to reaction, ΔG_R, accounting for non-ideality resulting from the chemical reaction of the two species that undergo mixing;
- Excess Gibbs free energy, ΔG_{ex}, which captures the non-ideal interactions developing upon mixing (without reaction) the two phases at stake.

The total Gibbs free energy of mixing is therefore given by:

$$\Delta G_{\text{mix}} = \Delta G_{\text{id}} + \Delta G_R + \Delta G_{\text{ex}} \tag{16}$$

For a system comprising NiOOH and Ni(OH)2 as the oxidized (Ni(III)) and reduced (Ni(II)) forms of Ni, with x representing the mole fraction of Ni(II), the free energy contributions are defined as:

$$\Delta G_{id} = RT\left[x \ln x + (1-x)\ln(1-x)\right] \tag{17}$$

where R is the gas constant and T is the absolute temperature.

$$\Delta G_R = x\mu^0_{II} + (1-x)\mu^0_{III} \tag{18}$$

where μ°_{II} and μ°_{III} are the standard chemical potentials of the equilibrium phase form of Ni(II)- and Ni(III)-containing species, respectively. This model does not account for chemical equilibrium, and simply describes for the free energy change of the system containing Ni(II) and Ni(III) in terms by connecting linearly the initial and the final states (pure and separated species in the equilibrium crystallographic forms).

$$\Delta G_{ex} = RT\left[x \ln \gamma_{II} + (1-x)\ln \gamma_{III}\right] \tag{19}$$

where γ_{II} and γ_{III} and are the activity coefficients of Ni(II)- and Ni(III)-containing species, respectively.

3.2.2 activity coefficient formulation

As hinted at above, the two-parameter Margules model provides a thermodynamic description of the non-ideality within the solid-state mixture of (reduced species,y) and (oxidized species,z). This approach treats the oxidized and reduced nickel species as distinct components of a binary solid solution [23, 24, 46, 47]. The mathematical expressions for the activity coefficients are derived from Wohl's expansion of the excess Gibbs free energy:

$$\frac{g^E}{RT} = x_1 x_2 \sum_{k=0}^{m} A_k \left(x_1 - x_2\right)^k \quad \text{with} \quad \ln\left(\gamma_i\right) = \left(\frac{\partial\left(\frac{n g^E}{RT}\right)}{\partial n_i}\right)_{T,P,n_{j\neq i}}$$

This method expands the excess energy into a power series of mole fractions where the coefficients represent the effective molecular sizes and the interaction parameters (including binary and ternary interactions) [24, 47]. By including higher-order terms compared to the one-parameter model, this formulation can describe more complex, asymmetric thermodynamic behaviors. [23, 48] Letting x represent the mole fraction of the reduced species, the activity coefficients are expressed as:
For Ni (II) ($x = 1$ corresponds to pure $Ni(OH)_2$):

$$\ln\left(\gamma_{\text{II}}\right) = A_0(1-x)^2 + B_0(1-x)^3.$$

For Ni (III) ($x = 0$ corresponds to pure NiOOH):

$$\ln\left(\gamma_{\text{III}}\right) = \left(A_0 + \frac{3}{2}B_0\right)x^2 - B_0 x^3.$$

In the polynomial expansion of these equations, the absence of constant and linear terms is dictated by fundamental thermodynamic constraints: (i)Zero Constant Term: Ensures that the activity of a pure species is equal to unity, (i) Zero Linear Term: Ensures that the derivative of the excess Gibbs energy vanishes at the limits of the pure components, satisfying the condition that the mixture behaves according to Raoult's Law in the limit of high concentration These expressions form the theoretical foundation for the model equations presented next. The inclusion of higher-order terms, such as cubic contributions, - not considered so far in the literature - allows the model to more accurately capture asymmetries and specific interaction effects within the mixture[23, 48]. Physically, the better fit provided by these higher-order terms suggests that the insertion of protons into the lattice occurs in an ordered, non-random fashion, which happens when all lattice sites are not equivalent [23**?**].

3.2.3 Physical Meaning of Parameters A_0 and B_0

As mentioned above, the Margules-type expansion, in fact, is a phenomenological polynomial expansion, without an explicitly underlying molecular-level model[24, 47]. Nevertheless, different orders in the expansion can be ex post associated with different physical effects or asymmetries in interactions, e.g., along the lines proposed in [23, 48] and summarized below. The relevant physical properties that can be associated with the parameters A and B are the following: (i) the effective ion size q; (ii) two-body interaction terms, assuming that there is only

one type of such interaction a and (iii) three-body interaction terms, assuming that there are two types of such interaction b1 and b2 [24, 47].In this formal framework, it is possible to define the parameters as follows:

$$A_0 = q(a + 2b_1 - b_2) \tag{20}$$

$$B_0 = q(2b_2 - 2b_1) \tag{21}$$

As described in [23, 24, 47], a large positive value of the interaction parameter indicates a thermodynamic repulsion between the two species, suggesting that the components are immiscible and tend toward phase separation. Mathematically, this contributes a linear term (with respect to the composition) to the chemical potential, effectively shifting the slope of the equilibrium curve. Conversely, the parameter accounts for the system asymmetry. This asymmetry arises from the fact that ternary configurations (e.g., 1-1-2 or 1-2-2) rarely possess the same interaction energy since the energy associated with a Ni(II)-rich triple differs significantly from that of a Ni(III)-rich environment.

3.2.4 Final expression of the reversible potential

The reversible potential is obtained by differentiating the total Gibbs free energy with respect to the mole fraction (x), and dividing it for nF[23, 24, 49]:

$$E(x) = -\frac{1}{nF}\frac{\partial G_M}{\partial x} \tag{22}$$

By substituting the expressions provided by the model for the activity coefficients and performing some straightforward algebraic manipulations, the two-parameter Margules model at constant pH can be restated as [23]:

$$E(x) = E_0 + \frac{RT}{nF}\ln\left(\frac{1-x}{x}\right) + \frac{RT}{nF}\left[A_0(1-2x) + B_0(1-6x+6x^2)\right] \tag{23}$$

Here, E_0 represents the standard potential, defined as $(\mu^0_{II} - \mu^0_{III})/nF$. The first two terms of this equation correspond to the ideal solution behavior (Nernst equation), while the third term, quadratic in x, directly accounts for the non-idealities.

3.2.5 Linear and quadratic parameters

The linear part of the third term of the previous equation, signifies the random insertion, as for the case of one-parameter Margules, while the higher order terms suggests that the insertion occurs in an ordered fashion, as shown by [23, 48]. The linear contribution of the third term indicates a random insertion of ions into the available crystallographic lattice sites. This behaviour relies on the assumption of equivalence, namely that the intercalated ions are randomly distributed over energetically equivalent lattice sites. Under this assumption, each site is statistically indistinguishable, and the occupation probability does not depend on local ordering effects[23, 48]. These linear terms account for several physical interactions among the intercalated species, including electrostatic repulsive and attractive forces arising between electrons and ions within the host lattice. In particular, the linear contribution reflects the shift of the Fermi level: the chemical potential of a solid is governed by the energy of the highest occupied electronic states, defined by the Fermi level. As the solid composition changes with x, the electronic structure evolves accordingly, and the linear term in the Margules-type model captures the first-order variation of this electronic energy. Additionally, ion insertion induces a local distortion of the electronic cloud and the surrounding atomic framework, giving rise to polarization effects. The linear term effectively represents the averaged contribution of these polarization interactions under the simplifying assumption that each newly inserted ion experiences a statistically identical chemical environment to that of previously inserted ions. Such an assumption is valid only in the case of a random distribution over equivalent lattice sites. The non-linear terms, instead, indicate that proton or ion insertion occurs in an ordered rather than random manner. The presence of these terms reflects non-ideal interactions among the intercalated species and implies the development of short-range ordering or site–site correlations within the host lattice[24, 47]. The inclusion of such higher-order contributions enables the two-parameter Margules model to reproduce the experimental data with significantly greater accuracy than simpler models. This improved agreement confirms that the structure of the active material, such as nickel hydroxide, promotes a structure-driven distribution of species, where the energetic cost of insertion is no longer uniform but depends on the local environment and the collective interaction between intercalated ions.

3.2.6 Fitting of experimental discharge-charge curves

To perform the fitting of the experimental data, two additional parameters, α and β, were introduced compared to the original model in order to shift the asymptotes away from the idealized values of 0 and 1. This adjustment is necessary because, in reality, the state of complete charge (DOD = 1) and complete discharge (DOD = 0) is never fully achieved due to irreversibility's and battery degradation [50].
The complete form of the equation used to fit the non-equilibrium curves is therefore:

$$V = E_0 + \frac{RT}{F}\ln\left(\frac{(x-\alpha)}{(x+\beta)}\right) + \frac{RT}{2F}\left(-2A + 4A(1-x) - 2B + 6B(1-x) - 3B(1-x)^2\right) \tag{24}$$

where $R = 8.314\ \mathrm{J\,mol^{-1}K^{-1}}$, $T = 298\ \mathrm{K}$, and $F = 96480\ \mathrm{C\,mol^{-1}}$.
For the fit of the quasi-equilibrium curve (data obtained from Amin's thesis), it was necessary to introduce a cubic term to the previously used expression, yielding the following equation:

$$V = E_0 + \frac{RT}{F}\ln\left(\frac{(x-\alpha)}{(x+\beta)}\right) + \frac{RT}{2F}\left(-2A + 4A(1-x) - 2B + 6B(1-x) - 3B(1-x)^2 + C(1-x)^3\right) \tag{25}$$

This modification can be considered as an expansion of the two-parameter Margules model in order to accurately describe the equilibrium behaviur. The model extension can be justified by stopping the Redlich-Kister equation at the fourth order instead of the third. Under these operating conditions (extremely low currents), the system remains in a state of quasi-equilibrium, allowing the "fine" thermodynamics of the material to emerge. In this regime, every subtle interaction between the intercalated ions has sufficient time to manifest and influence the electrode potential—effects that would otherwise become negligible at higher currents. Because these interactions differ significantly between and species, the resulting potential-composition curve exhibits a pronounced asymmetry between the charged and discharged states. This behavior necessitates the use of higher-order terms, such as the cubic term in the two-parameter Margules model, to accurately capture the energetic landscape of the host lattice.
Although the acquired data do not strictly represent the thermodynamic equilibrium curve, the magnitude of the current is sufficiently low to justify a quasi-equilibrium approximation. This approach is particularly valid at lower current densities, where more pronounced asymmetries and distinct curvatures emerge, especially at low stoichiometric values of x. At low discharge currents, Zn–Ni batteries operate close to thermodynamic equilibrium; in this regime we have that: the ohmic overpotential is negligible due to the low current flowing through the internal resistances of the cell, the ionic diffusion is not rate-limiting, since concentration gradients in the electrolyte and within the electrode are weak or absent. In addition to that, at low current density the system works in the linear region of the Butler-Volmer equation and so the activation energy (the activation energy responsible to decrease the energy barrier allowing the flow of the electron and so higher current density) is very low, so we have that:

$$E = E_0 + \eta_\Omega + \eta_{att} + \eta_{diff} \tag{26}$$

$$\eta_\Omega \approx \eta_{att} \approx \eta_{diff} \approx 0 \tag{27}$$

Once the optimal fitting expression for the nickel electrode was established, two additional input parameters were incorporated into the model: DOD_{min} and DOD_{max}, defining the lower and upper limits of the admissible depth-of-discharge window. In practical applications, battery operation does not typically involve complete charge and discharge cycles. Instead, cycling is constrained within predefined depth-of-discharge limits to avoid excessive degradation and to ensure operational safety.
Consequently, the charge curve is no longer evaluated over the entire theoretical DOD range, but is instead restricted to the interval

$$\mathrm{DOD} \in [\mathrm{DOD}_{min}, \mathrm{DOD}_{max}] \tag{28}$$

Thus, the resulting charge and discharge profiles corresponds to a truncated segment of the original fitting function, representing the effective operational window of the electrode under realistic cycling conditions:

$$V = E_0 + \frac{RT}{F}\ln\left(\frac{(t-\alpha)}{(t+\beta)}\right) + \frac{RT}{2F}\left(-2A + 4A(1-t) - 2B + 6B(1-t) - 3B(1-t)^2 + C(1-t)^3\right) \tag{29}$$

$$t = (DOD_{min} + (DOD_{max} - DOD_{min})x) \tag{30}$$

and for the discharge:

$$t = ((1 - DOD_{max}) + (DOD_{max} - DOD_{min})x) \tag{31}$$

3.2.7 Definition of the new boundary condition for the Ni electrode in the modified MAC model

To define the new boundary conditions for the asymmetric cell, the MAC model code was modified at $x = L$, while the boundary conditions at $x = 0$ were left unchanged.
The zinc flux derivative was set equal to zero at the nickel electrode, assuming that no zinc-ion flux occurs at this interface:

$$\frac{\partial u}{\partial x} = 0 \text{ at } x = L \tag{32}$$

Accordingly, the boundary condition at the nickel electrode becomes:

$$-\frac{zDF}{RT} u(x = L, t) \left.\frac{\partial \phi}{\partial x}\right|_{x=L,t} = \frac{i(t)}{zF} \tag{33}$$

where $\phi(i, t)$ is now a known quantity derived from the analytical expression previously obtained:

$$\phi(i,t) = E_0(i) + \frac{RT}{F} \ln\left(\frac{t-\alpha}{t+\beta}\right) + \frac{RT}{2F}\left[-2A(i) + 4A(i)(1-t) - 2B(i) + 6B(i)(1-t) - 3B(i)(1-t)^2 + C(i)(1-t)^3\right] \tag{34}$$

The potential at the nickel electrode is no longer a function of the concentration u; furthermore the Nichel electrode is not subject to passivation or dendritic growth, as it operates via solid-state intercalation. Consequently, the nickel electrode's capacity for charge exchange does not decay over time due to morphological degradation, maintaining a stable active surface area throughout the process, so the current density at the cathode is:

$$I(t) = \mid i(t) \mid \tag{35}$$

3.2.8 Fitting parameters equation

The dependence of the fitting parameters $A(i)$, $B(i)$, and $E_0(i)$ on the applied current was determined empirically by interpolating their values obtained at the different current densities investigated experimentally.
Specifically, the analysis of the discharge curves revealed that the equilibrium potential parameter, , exhibits a trend closely resembling that of the total overpotential [51]. Consequently, its behavior was modeled as:

$$E_{\text{cell}}(i) = E_{\text{eq,cell}} - \eta_{CT}(i) - \eta_{\Omega}(i) - \eta_{MT}(i) \tag{36}$$

which can be expressed explicitly as:

$$E_{\text{cell}}(i) = E_{\text{eq,cell}} - B \ln\left(0.5(\frac{i}{i_0} + \sqrt{\left(\frac{i}{i_0}\right)^2 + 4}\right) - Ri + \eta_{MT}(i) \tag{37}$$

where:

- $\eta_{\Omega}(i)$ represents the ohmic contribution (resistive losses),
- $\eta_{CT}(i)$ describes the charge-transfer kinetics,
- $\eta_{MT}(i)$ accounts for mass transport limitations.

For the specific case considered here, the mass transport term $\eta_{MT}(i)$ was neglected, as at the relatively low applied currents, the corresponding diffusion limitations, are negligible.
For the charge curves, the parameter $E_0(i)$ exhibits an almost linear trend with respect to the applied current. Since the experimental behavior is essentially linear, it can be assumed that the system operates in an ohmic regime, where activation effects are negligible compared to the resistive voltage drop.
In this case, the voltage-current relationship can be approximated by Ohm's law, $V = RI$. This suggests a relatively high exchange current density i_0, indicating fast electrochemical kinetics and rapid charge-transfer reactions. For this reason, the fitting procedure was carried out using a simple linear relationship of the form

$$y = mx + q.$$

Within the cell, additional effects must also be considered. These are incorporated through empirical coefficients $A(i)$ and $B(i)$, which account for the modifications in the reaction mechanism, variations in the electrochemical double layer structure and other system-specific nonlinearities.
The fitting of parameters $A(i)$ and $B(i)$ was performed using exponential functions of the form:

$$A(i) = C + De^{-i/k} \tag{38}$$

The details regarding the fitted curve are provided in Appendix A.

3.2.9 Definition of the total cell voltage

To conclude the formulation of the mathematical framework, it is necessary to define how the electrode potentials derived from the boundary conditions are translated into the measurable cell voltage for both investigated systems.

3.2.10 Symmetric cell configuration

For the symmetric Zn/Zn configuration, all characteristic voltage transients are described by summing the contributions of the activation overpotentials at both interface:

$$\Delta\Phi = B\ln\left[0.5\left(\frac{|i(x=0)|}{i_0} + \sqrt{\left(\frac{i(x=0)}{i_0}\right)^2 + 4}\right)\right] + B\ln\left[0.5\left(\frac{|i(x=L)|}{i_0} + \sqrt{\left(\frac{i(x=L)}{i_0}\right)^2 + 4}\right)\right] \tag{39}$$

This expression allows for the accurate representation of symmetric voltage transient profiles by specifically taking into account the differences in current density at the two boundary conditions.

3.2.11 Full-cell configuration

In the case of the extended MAC model for the Ni-Zn full-cell, the equation used to compute the final voltage curves is modified to account for the asymmetric nature of the system:

$$\eta_{an}^{CT} + \eta_{cat}^{CT} = B\frac{I}{|I|}\left\{\ln\left[\frac{1}{2}\left(\frac{|i(x=0)|}{i_0}\right) + \sqrt{\left(\frac{i(x=0)}{i_0}\right)^2 + 4}\right]\right\} \tag{40}$$

In this formulation, the term specifically related to the cathode charge transfer overpotential has been eliminated. This simplification is justified because the cathodic activation contribution is already implicitly accounted for within the new potential boundary conditions derived from the Margules thermodynamic formalism.

.

4. Materials and Methods

4.1. NICKEL CATHODES: MATERIALS AND ELECTROCHEMICAL MEASUREMENTS

4.1.1 Ni/NiOOH cathode extraction

Ni/NiOOH cathode material is extracted from Ni-MH AA-energizer 2000mAh commercial batteries through a carefully controlled procedure to preserve the structural and electrochemical integrity. The batteries were first discharged at a C/10 rate to a cutoff potential of 0.15 V to minimize the risk of short-circuiting during subsequent handling and disassembly. Following discharge, the battery casing was removed using a handheld precision Dremel. The cathode material was extracted from the top of the cell, unrolled, and cleaned with deionized water (DI-W). To enhance the mechanical stability and ensure uniform surface characteristics, the extracted cathode was subjected to two pressing protocols: cold pressing at 500 psi for 1 minute, followed by hot pressing at 80°C for 5 minutes at 500 psi. The cathodic material was then punched to disk of 18 mm of diameter.
Here is reported the potential of the battery during the discharge:

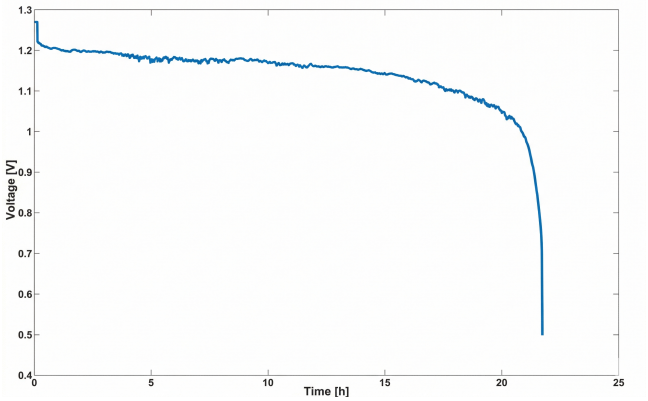

Figure 1: Ni-MH AA-energizer discharge curve

4.1.2 Chronopotentiometry (CP)

CP were performed in a three-electrode cell, using an Hg/HgO reference electrode (AMEL 383/OHG/12, 0.1 M KOH) a 0.9 cm^2 platinum counter electrode (CE). Extracted Ni/NiOOH was mounted in a PTFE sample support with three sealing gaskets (595/SH & 3x 595/SS, AMEL) and complete support stand (591/BASE & 591/COBO, AMEL) and used as Working electrode (WE). The cell contained 200 mL of 6 M KOH.
To characterize the electrode behaviour, three sets of measurements were carried out:
The first set of measurements was conducted by maintaining a constant charging current of 1.5 mA, followed by a series of discharges carried out at the following currents, in order: 0.5 mA, 3 mA, 0.38 mA, 6 mA, and 0.76 mA.
Two potential cut-offs were set for the charge and the discharge of the cathodic material (0.5V and 0.1V vs Hg/HgO respectively). At the end of each measurement, an aliquot of fresh electrolyte was employed. The RE and all the cell components were thoroughly washed the deionized water.
Subsequently the battery was discharged at the same current of 1.5 mA, while multiple charging steps were performed at different current values 0.3 mA, 0.6 mA, 1.5 mA, 3 mA. As in the previous case, a cut-off voltage of 0.5 V vs Hg/HgO was applied, along with a time limit of 60 hours.
To effectively evaluate the experimental data additional measurements were carried out while keeping the charging current fixed at 1.5 mA. In this set of tests, the battery was discharged using the following currents, (this time applied in increasing order), 0.6 mA, 0.75 mA, 1.2 mA, 3 mA, and 6 mA. For the cutoff were used the same condition as before.

4.1.3 definition of discharge and charge cutoff value

Once the experimental setup was established, it was necessary to define the charge and discharge cut-off voltages. According to the article [52], several key factors must be considered in order to determine the optimal potential window:
Redox activity: after performing a series of CV, using $Ni(OH)_2$ electrode Vs Hg/HgO, the best range of potential were between 0 and 0.55 V. This choice is motivated by the fact that the intense redox peaks, associated with the battery-type behavior of the materials, occur precisely within this potential range.
Discharge plateau: In galvanostatic charge discharge (GCD) tests, it was observed that the voltage plateau where the majority of charge transfer occurs terminate at specific potentials, namely around 0.14 V for α-$Ni(OH)_2$ and 0.19 V for β-$Ni(OH)_2$. Setting the discharge cut-off slightly below these values allows the full capacity of the material to be captured while avoiding potential regions where no significant electrochemical activity takes place.
It is also important to avoid electrolyte (KOH) decomposition which might occur at to high charge potential (usually above 0.6 V), were oxygen evolution reaction could starts; in addition to that, exceeding this limit would lead to an increase in current that does not contribute to energy storage within the material, but instead promotes gas evolution, thereby reducing the faradaic efficiency and potentially causing structural degradation of the electrode.

4.2. SYMMETRIC Zn CELLS WITH ZWITTERION ADDITIVES: experiement set up

April experiment

For the experiments on symmetric Zn/Zn cells, a total of 30 coin cells were assembled, corresponding to 10 replicates for each additive investigated: for the electrodes were used standard metallic cases characterized by 1.2 cm of diameter. The electrolyte consisted of an aqueous solution containing 2 mol of $ZnSO_4$ and 0.003 mol of additive, dissolved in 500 mL of deionized water (volume used for the experiment 80 μL). As separator glass fiber 260 was used with a micron thick and a diameter of 19 mm. All the elements were then assembled and pressed together.
Three different additives were tested: NBSD-195, NBSD-201, and NBSD-257. The assembled cells were sealed, mechanically pressed, and subjected to galvanostatic cycling at a current of 0.7 mAh/cm^2, for a total of 3 h per cycles.

August experiment

The experiment was repeated a second time using 30 coin cells containing the same three additives. In this set of measurements, the applied current density and the cycling protocol were modified. Specifically, for the first group of cells, a current density of 1 mA cm^{-2} was applied with galvanostatic charge and discharge steps of 1 h each. For the second group, the current density was increased to 5 mA cm^{-2}, while maintaining the same charge and discharge duration of 1 h.

4.2.1 SYMMETRIC CELL WITH DIFFERENT CUTS TECNIQUES

To further assess the robustness and general applicability of the proposed shape-classification method, an additional set of cells was tested under modified operating conditions, characterized by a shorter cycling period of 24 minutes and an applied current density of 1 mA cm^{-2}. A total of 30 cells were fabricated for this purpose: 10 produced by laser cutting, 10 by mechanical punching, and 10 by shielded-punching, enabling a comparative evaluation across different manufacturing processes.

4.2.2 SYMMETRIC CELL with DES Electrolyte

Symmetric Zn|Zn cells were assembled in coin-cell configuration using a $ZnSO_4$:EG deep eutectic solvent (DES) electrolyte[53]. Galvanostatic cycling was performed at 0.5 mA cm^{-2} with 30 min/30 min plating/stripping. Additional continuous cycling tests were carried out at 0.8 mA cm^{-2} for 3 h per half-cycle. In selected experiments, cycling was conducted at 0.8 mA corresponding to 2.4 mAh (2.12 mAh cm^{-2} referred to the Zn foil), with a depth of discharge (DOD) of 2. Long-term stability was evaluated up to 391 h (65 cycles) and 862 h (144 cycles), with reports of 400–450 cycles under the stated conditions..
Symmetric Zn|Zn cells in aqueus condition (AQ), were cycled at 0.8 mA cm^{-2} for 3 h per half-cycle.

4.3. FULL CELLS WITH Zn ANODES

4.3.1 Hot pressed and blade coated electrodes

All the experimental data are taken from:[3]
The charge–discharge performance of the nickel–zinc cells was evaluated using two ZnOC nanoparticle–based anodes fabricated by different processing methods: blade coating (thickness $\approx$ 100 μm) and hot pressing (thickness $\approx$ 400 μm). A commercial Ni/NiOOH cathode, extracted from Ni–MH AA batteries, was employed as the counter electrode.
The electrolyte consisted of a 6 M KOH aqueous solution, used in a limited volume (100 μL), without the addition of additives or ZnO saturation, in order to reproduce practical and deliberately "harsh" operating conditions.
Electrochemical measurements were carried out in both standard CR2032 coin cells and in a split-cell configuration. For both charge and discharge processes, a 1C rate was applied. The cells were charged up to the theoretical capacity of ZnO, with an upper cut-off voltage of 2.1 V and a maximum charging time of 1 h. Discharge was performed with a lower cut-off voltage of 1.35 V.
Thin electrodes were tested at 100% depth of discharge (DOD), whereas thicker electrodes were evaluated at 10% DOD.

4.3.2 FULL CELL with Zn Anode and Different Cathode (TQC, CMC)

Full Zn|TQC cells were assembled using Zn foil in combination with CMC. Galvanostatic cycling was performed at 0.8 mA with a capacity of 2.4 mAh (2.12 $\mathrm{mAh\,cm^{-2}}$ referred to Zn foil), corresponding to a Zn DOD of 2%, delivering 200 $\mathrm{mAh\,g^{-1}}$ and 180 $\mathrm{mAh\,g^{-1}}$ over 185 cycles (Exp-1).
Additional experiments were conducted at 1.5 mA with 5.3 $\mathrm{mAh\,cm^{-2}}$ (Zn foil DOD 3%), reaching 250 $\mathrm{mAh\,g^{-1}}$ over 20 cycles (Exp-4) . A further test at 1.5 mA and 4.5 $\mathrm{mAh\,cm^{-2}}$ (Zn foil DOD 3%) was reported as running .

4.3.3 FULL CELL with DES Electrolyte

Full cells employing $ZnSO_4$:EG DES electrolyte were assembled in coin-cell configuration. Galvanostatic cycling was performed at 0.8 mA corresponding to 100 $\mathrm{mAh\,g^{-1}}$, using electrodes with a mass of 0.0081 g (coin cells 1–3, Exp-2) .
In DESEG 50% systems, full cells were tested at 0.549 mA (100 $\mathrm{mAh\,g^{-1}}$, electrode mass 0.0061 g, Svit cell, Exp.1). Coin cells (cells 4–6) were cycled at 0.81 mA corresponding to 100 $\mathrm{mAh\,g^{-1}}$ with electrode mass 0.0081 g (Exp.1). Additional TBAB-based systems were tested in coin-cell configuration (cells 7 and 8, Exp.2).
Reported cycling interruptions due to short circuit and passivation events occurred at 138 h (23 cycles), 246 h (41 cycles), and 398 h (66 cycles) .

5. RESULTS AND DISCUSSION

5.1. CELL-VOLTAGE TRANSIENT (V(t)) CLASSIFICATION FOR EXPERIMENTAL TIME SERIES

The overarching objective of this research is the automated parametric identification for battery GDC time-series based on the MAC model, accounting for metallic anode morphology development and mass-transport in the electrolyte, employing a general intercalation cathode. Prior investigations on the MAC model for symmeric cells [4, 25] have demonstrated that, for diagnostic and monitoring purposes, the determination of an exact parameter vector is neither necessary for system monitoring nor necessarily physically meaningful, owing to the expected presence of Numerical Global Minima (NGM) [54]. In fact, in morphology-driven systems, the mapping between parameter sets and voltage transients is intrinsically non-unique: multiple combinations of transport coefficients, kinetic constants and morphological descriptors can generate qualitatively indistinguishable electrical responses. Consequently, classical pointwise curve fitting may yield parameter estimates that are numerically precise but physically non-identifiable. On this basis, the present work adopts a regime-based identification strategy. Rather than targeting the exact reconstruction of individual voltage curves – an approach that has been pursues previously in our group [11, 12], the present analysis focuses on the classification of transient morphologies and on the determination of the corresponding admissible regions in parameter space. In this framework, each characteristic waveform is not associated with a single parameter vector, but rather with a finite multidimensional domain, i.e. a hypervolume, within the space of governing parameters. The objective of this section is therefore twofold: (i) to systematically identify the morphological families emerging from experimental data and the MAC model and (ii) to map the hypervolumes of parameter space responsible for their generation. This approach shifts the emphasis from exact numerical matching toward the identification of electrochemical behavior classes, thereby enabling a robust interpretation of voltage transients in terms of dominant physical mechanisms. Such a formulation offers several advantages. First, it mitigates the issue of structural non-uniqueness inherent to inverse problems in nonlinear electrochemical systems. Second, it enhances robustness against experimental variability, as classification relies on qualitative waveform features rather than pointwise agreement. Third, it establishes a direct connection between transient morphology and underlying transport–kinetic regimes, facilitating the interpretation of degradation pathways in both symmetric and full-cell configurations.

5.1.1 Euristic transient shape classification

An exhaustive inspection of the experimental voltage time series was performed prior to any model-based interpretation, with the objective of identifying recurring qualitative features in the galvanostatic transients. Rather than relying on integral descriptors, such as time-to-failure, the analysis focused on the intrinsic morphology of individual semi-periods, thereby extracting physically meaningful information embedded in the voltage evolution. Each half-cycle was examined independently, in order to isolate the evolving dynamic behavior under constant current conditions. This systematic inspection revealed that the vast majority of experimental responses can be classified into four fundamental transient morphologies, as detailed in the following subsection.

It is worth noting that, although the vast majority of transients fall within the four fundamental morphological families described above, additional irregular or "messy" waveforms were occasionally observed. These typically appear after the onset of a soft short-circuit or in close proximity to the final short-circuit event. Such signals exhibit abrupt slope variations or mixed curvature patterns that prevent unambiguous classification. From a functional standpoint, however, these unclassified transients appear consistently associated with advanced degradation states, namely cells that are already compromised or close to failure. In this sense, the "unclassified" category can still be assigned a clear physical meaning, as it corresponds to pathological operating regimes rather than to distinct, stable electrochemical behaviors.

5.1.2 Symmetric cell shape classification

Inspection of symmetric-cell transients yielded the four fundamental morphological families, schematized:

	MAC model	Symmetric cell	Full cell
SHAPE 1	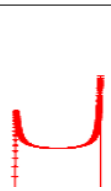		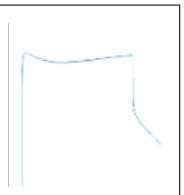
SHAPE 2	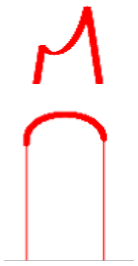		
SHAPE 3	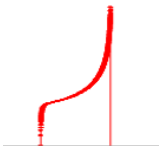		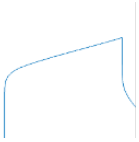
SHAPE 4		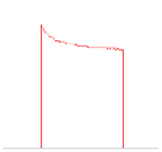	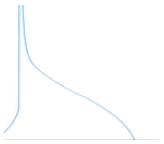

Table 1: waveform comparison

Shape 1 – Single Minimum. This waveform is characterized by an initial decrease in voltage reaching a well-defined minimum, followed by a recovery toward higher values within the same semi-period. Shape 2 – Extremum Reversal (Minimum–Maximum or Maximum). This morphology exhibits the presence of two distinct curvature regions, typically a minimum followed by a maximum, or in some cases a pronounced maximum alone. Shape 3 – Monotonically Increasing Profile. In this case, the voltage increases continuously throughout the semi-period without internal extrema. Shape 4 – Monotonically Decreasing Profile. This transient is characterized by a continuous voltage decrease over the entire semi-period.

5.1.3 Transient shape classification for full cells

The extension of the analysis to full Zn–Ni cells introduces an intrinsic asymmetry absent in the symmetric configuration. While the zinc electrode remains governed by morphology-driven transport and kinetic effects, illustrated in Section 2.2, the nickel electrode operates through solid-state intercalation, modelled in Section 3.2. As a result, the voltage transient reflects the superposition of two fundamentally different electrochemical responses. Despite this structural asymmetry, the full-cell waveforms can still be qualitatively classified according

to the same four morphological families identified for symmetric cells (see Section 5.1.1.1). However, the charge and discharge semi-periods must be analyzed separately owing to their distinct dynamical behaviors. Thus, in full cells, the following features were observed. The morphological classification for full-cell transients reveals that Shape 3 is the predominant configuration, appearing with high regularity in both positive and negative semi-periods. It is important to notice taht, in experiments utilizing the TQC cathode, Shape 3 appears with a high degree of symmetry across both positive and negative semi-periods. Shape 4 is generally observed during negative transients but remains significantly less recurrent than Shape 3 in the experimental datasets. Finally, Shapes 1 and 2 are rare within the full-cell framework, appearing only within limited regions of the parameter space or under specific operating conditions

5.1.4 Algorithm for automatic transient shape classification

Once the classification framework had been established, a MATLAB code was developed to automatically identify the characteristic shapes within the experimentally measured voltage transients. To ensure robust detection and to avoid misclassification due to spurious local extrema occurring near the switching points, each half-period was processed individually within a loop structure. For shape-identification robustness, a margin was excluded at both the beginning and the end of each semi-period. Importantly, this excluded interval was not defined as a fixed absolute time, but was scaled according to the total duration of the semi-period. As a consequence, it is possible that some waveforms characterized by a peak occurring very close to the beginning of the semiperiod may be classified as Type 4 rather than Type 2. Similarly, in the presence of negative peaks occurring near the beginning of the interval, the waveform may be identified as Type 3 rather than Type 1.
The remaining portion of the signal was subsequently partitioned into six equal sub-intervals.
The half-period was then classified according to the sign pattern of these mean derivatives, following a rule-based logical scheme, described in the Algorithm 1.Specifically, the sign combinations were used to assign the transient to one of the four previously defined shape categories, while signals not satisfying any predefined condition were labelled as "unclassified."
Short-circuit events and passivation phenomena were identified using threshold-based criteria. If the average voltage over a half-period fell below a predefined lower threshold, the signal was classified as a short circuit. Conversely, if the average voltage exceeded an upper threshold, the condition was attributed to passivation. In the final graphical representation, these two additional categories were denoted as Shape 5 (short circuit) and Shape 6 (passivation), respectively.
The output of the algorithm consists of a plot reporting the classified shape along the y-axis as a function of the half-period index on the x-axis, thereby providing a time-resolved visualization of the evolution of transient behavior throughout the experiment, like is shown in the following figure:

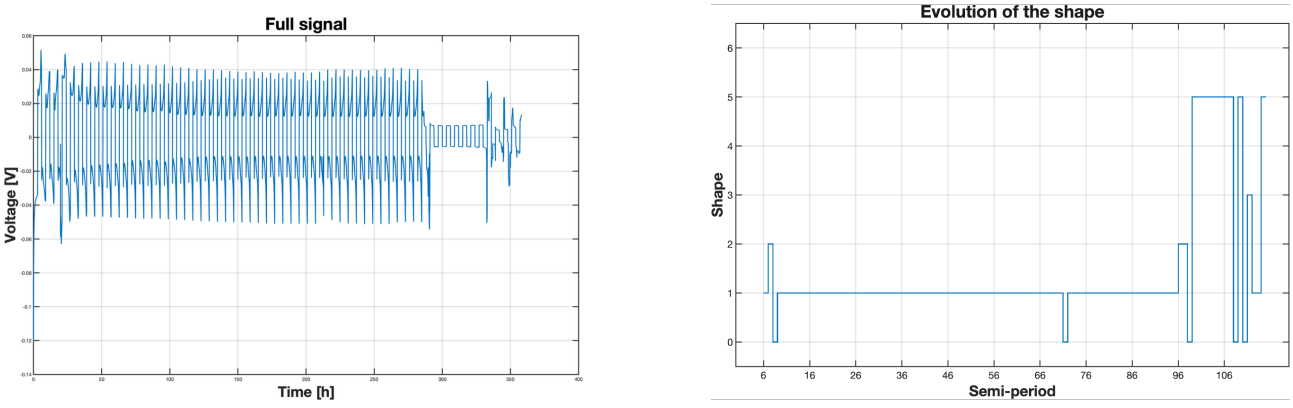

Figure 2: Shape recognition.

5.1.5 Algorithm for shape recognition of voltage transients for symmetric cells

The model described in section 5.1.4 was then applied on real voltage transition. In the case of symmetric Zn|Zn cells, the voltage signal naturally crosses zero at each current reversal. This property allows the negative semi-periods to be analyzed by considering the absolute value of the voltage signal.
The use of $|V(t)|$ was therefore adopted as a signal-processing choice rather than as a physical assumption of symmetry. While the cell configuration is symmetric, the transient morphologies themselves may still exhibit intrinsic asymmetries due to transport and kinetic effects. However, since the voltage changes sign between consecutive half-cycles, operating on the modulus enables a unified application of the same derivative-based

classification criteria to both positive and negative semi-periods. Additional explanatory plots of the model can be found in Appendix A.3.

5.1.6 Algorithm for shape recognition of voltage transients for full cell

The shape recognition algorithm, originally developed for symmetric cells (Section 5.1.4), is equally applicable to full-cell configurations. However, a key distinction arises in the temporal domain: in a classical full cell cycling experiment, a voltage cut-off is set as an additional criterion for switching between discharge and charge periods, rather than a fixed discharge/charge time, which is the typical case for symmetric cells. As a consequence, the semi-period durations, in general, are no longer fixed, but exhibit variable durations dictated by the specific voltage cut-off or time limits imposed during the testing. This experimental characteristic can, in principle, be straightforwardly accounted for in the MAC model, but this would require a major coding retrofit, that is beyond the scope of the present paper. Moreover, unlike the symmetric-cell case, the use of absolute voltage values for transient analysis is no longer suitable, since the cell potential does not cross zero. Consequently, the classification logic was modified by inverting the sign of the mean derivative during the negative semi-periods. This slight algorithmic modification, of course, preserves consistency in the classification criteria. To identify the characteristic asymmetries between charge and discharge processes for the full cell case, two separate plots were generated for the charge and discharge segments, respectively.
Additional explanatory plots of the model can be found in Appendix A.4.

5.2. Automated transient shape classification for experimental data

Following the heuristic identification of the four principal waveform families, the automated classification algorithm was applied to the carry out a systematic analysis of experimental dataset. The objective of this step is still agnostic to the physical origin of the transients, and aims at systematically comparing and grouping the observed waveform morphologies over cycling time and across varied experimental conditions.
Below, the classification results will be presented according to the type of experiment performed.

5.2.1 Symmetric Zn–Zn cells with zwitterionic additives and different current densities

For the dataset comprising symmetric cells containing different additives (NDSB-195, NDSB-201, NDSB-257),(see Section 4.2), the automated classification revealed a predominant occurrence of Shape 1 during the early and intermediate stages of cycling. As cycling progressed, an increased frequency of Shape 3 was observed in several cells, particularly prior to short-circuit events.
When the data were aggregated by additive type, clear statistical differences emerged in terms of the relative frequency and temporal persistence of the different waveform classes. NDSB-195 additives exhibited longer sequences dominated by a single morphology, whereas NDSB -201 and 257 displayed more frequent transitions between shapes before failure, as shown in the figure:

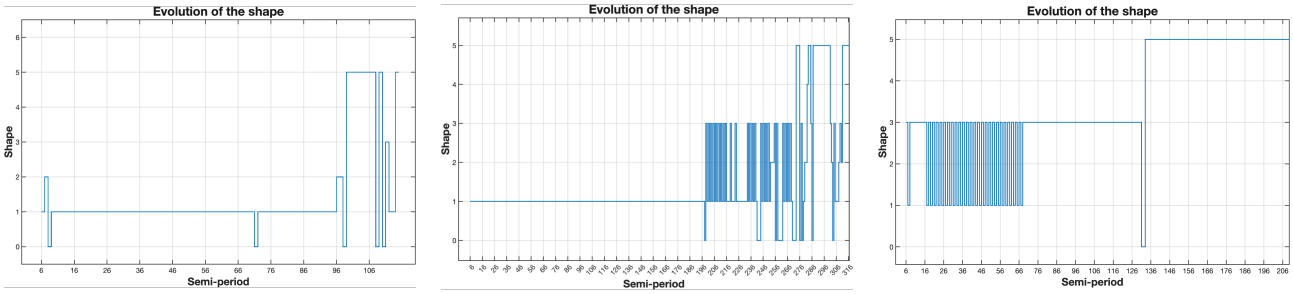

(NDSB-195) (NDSB-201) (NDSB-257)

Figure 3: Waveform class persistence by additive type.

As far as the dependence of applied current density (0.7, 1, and 5 mA cm^{-2}) is concerned: a systematic variation in the distribution of waveform classes was observed. Higher current densities were associated with shorter sequences of stable morphological patterns and earlier transitions toward monotonic profiles (Shape 3 or Shape 4).
The automated classification thus enabled a direct comparison between operating conditions, highlighting how the relative proportion of waveform families changes as a function of applied load.

5.2.2 Symmetric cells with different electrode fabrication methods.

As detailed in Section 4.2.1Materials and Methods, symmetric cells were used to test the impact on Zn cyclability of mechanically punched, shielded-punched, and laser-cut electrodes. In this case, even though the fabrication mode has a marked impact on the time-to-short circuit, the transient classification algorithm revealed a high degree of uniformity in the dominant waveform class, irrespective of the fabrication techniques. Shape 3 was the most frequently identified profile during regular operation, while Shape 4 typically appeared after short-circuit events.
Nevertheless, subtle differences were observed in the frequency of "unclassified" transient, particularly immediately after failure events. These differences are attributable to signal irregularities rather than to distinct morphological categories.

Experiment	**Cause of failure**	**Characteristi shape**	**Change of shape before failure**	**Restart with defined shape after failure**	**replicates**
NDSB 195 1 mA/cm^2	Short circuit	Shape 1	no	no	5/5
NDSB 201 1 mA/cm^2	Short circuit	Shape 1	shape 3 with shape 1	shape 1 with 3	3/5
NDSB 257 1 mA/cm^2	Short circuit	Shape 1	Shape 3	shape 3 with 1	5/5
NDSB 195 5 mA/cm^2	Short circuit	Shape 1	no	no	5/5
NDSB 201 5 mA/cm^2	Short circuit	Shape 1	no	no	5/5
NDSB 257 5 mA/cm^2	Short circuit	Shape 3	Shape 1 with 3	no	3/5
Punched	Short circuit	Shape 3	no	Shape 3	7/10
Shield punched	Short circuit	Shape 3	no	Shape 3	6/8
Laser cut	Short circuit	Shape 3	no	Degenerate shape 1 and 3	8/9

Table 2: Summary of experimental and failure characteristics.

5.2.3 Additional data of symmetric cells

To test the generality and robustness of the proposed model and the associated morphological classification framework, the method was further validated against a diverse set of electrochemical conditions, detailed in Section 4.2.2). Specifically, the model was tested on experiments performed: (i) with various electrolytes and electrolyte additives; (ii) with different electrode surface treatments and (iii) at different applied current densities. This showed the generality of the approach, notably extending the application portfolio.

Experiment	Couse of failure	Characteristi shape	Change of shape before failure	Restart with defined shape after failure	replicates	Time to failure [h]
CMC	Short circuit	Shape 3	no	no	2	180 h 50 h
DESEG 40%	Short circuit	Shape 3	no	Shape 3 (1/2)	2	100 h 50 h
ZnSO4 DESEG	Passivation (2/3)	Shape 3	no	no	3	2200 h 400 h 1500 h
TBAB	Short circuit	Shape 1 and 3	no	Shape 1 and 3 (2/3)	3	100 h 185 h 20 h
AQ	Short circuit Passivation at the end of mensuration	Shape 1	no	Shape 1 (2/6)	6	$300 \pm 74,4$

Table 3: Experimental results for different electrolytes and additives.

5.2.4 Full cells with Zn anodes and nickel cathodes

As put forward in Section 5.1.3, in the case of full-cells the classification was performed separately for charge and discharge semi-periods due to their intrinsic asymmetry. Specifically, as far as Zn-Ni cells are concerned (see Section 4.3), the automated analysis showed that Shapes 3 is the dominant class under practical cycling conditions, with fewer occurrences of shape 4 and 2 which are typically observed in close proximity to cell failure.

5.2.5 Full cells with Zn anodes and organic cathodes

When organic cathode materials are employed, such as TQC (see Section 4.3.2), the experimental voltage transients exhibit a high degree of symmetry between the charge and discharge semi-periods. In these configurations, Shape 3 remains the predominant waveform for both anodic and cathodic processes throughout the operational life of the cell.
Unlike the Ni-Zn system, these curves do not show a pronounced asymmetry. The overall voltage profile is characterized by a monotonic evolution, shape 3, that remains relatively consistent in both semi-periods, indicating that the organic cathode does not significantly alter the transient dynamics or introduce additional curvature signatures. This behavior confirms that the system remains primarily governed by the transport-limited regimes of the zinc electrode, while the organic cathode maintains a stable and non-interfering electrochemical response under the investigated conditions. Additional explanatory plots of the model can be found in Appendix A.4.

Experiment	Cause of failure	Characteristi shape	Change of shape before failure	Restart with defined shape after failure	Replicates
ZnSO4_DESEG 2M	Passivation (2/3)	Shape 3	No	1/3	2/3
ZnSO4 DESEG 50%	Passivation	Shape 3	No	No	3/3
ZnSO4 DESEG +TBAB	Passivation	Shape 3	Shape 1 (degenerate)	No	2/2
Splitcell CMC + TBAB TQC cathode	Short circuit	Shape 3	No	No	1/1
Split cell	Short circuit	Shape 3	No	Shape 3	1/1
Svit cell	Short circuit	Shape 3	No	Shape 3	1/1
Swadgelock griphiterod CMC+TOCspesso	Short circuit	Shape 3	No	No	1/1
Hot pressed	Short circuit	Shape 3	No	No	1/1
Blade coating	Short circuit	Shape 3	No	No	1/1

Table 4: Experimental summary of full cell configurations.

5.2.6 Conclusions on transient shape classification for experimental data

Overall, the automated transient shape classification provides a structured and reproducible method for organizing large experimental datasets into a limited number of morphological families. By grouping results according to additive type, current density, fabrication method, and cell configuration, it becomes possible to compare experimental conditions on a common categorical basis, independently of detailed physical interpretation. This classification framework thus serves as a statistical bridge between raw voltage time series and the subsequent parameter-regime analysis.

Importantly, the classification results confirm that the four fundamental waveform families identified within the MAC theoretical framework are not merely numerical artifacts of the model, but emerge consistently in real experimental data, both in symmetric and full-cell configurations. This correspondence strengthens the physical interpretability of the model and supports the validity of morphology-based voltage analysis as a diagnostic tool.

Shape 1 is predominantly observed in symmetric $Zn - Zn$ cells during the early and intermediate stages of cycling at moderate current densities (e.g., 1 mA cm^{-2}), particularly in the presence of zwitterionic additives. It is also frequently detected in aqueous symmetric systems. In these configurations, this morphology is typically associated with regular and stable transient behavior, reflecting a balanced electrochemical regime during cycling.

Shape 2 is comparatively rare in the experimental datasets and appears only within restricted parameter ranges. In symmetric cells, it is observed predominantly after cell failure, whereas in full-cell configurations it tends to emerge shortly before failure. This behavior suggests that the occurrence of Shape 2 may signal the onset of critical morphological instabilities, such as significant surface restructuring or localized growth phenomena, which typically precede short-circuit events.

Shape 3 in the symmetric configuration, becomes increasingly prevalent either at higher current densities (e.g., 5 mA cm^{-2}) or in the later stages of cycling. In several datasets, the transition from Shape 1 to Shape 3 precedes short-circuit events. Shape 3 is the most frequently observed morphology under practical operating conditions in full cells system; its symmetry varies significantly depending on the cathode chemistry. Specifically, full cells utilizing TQC organic cathodes exhibit a high degree of symmetry, with Shape 3 manifesting consistently in both positive and negative semi-periods. This suggests that the TQC cathode does not significantly influence the transient dynamics, leaving the overall voltage profile governed primarily by the zinc electrode. Conversely, systems employing nickel cathodes are characterized by more irregular and pronouncedly asymmetric transients. This asymmetry originates from the coupling of morphology-driven zinc dynamics with the complex solid-state intercalation thermodynamics of the nickel electrode, which fundamentally differentiates the charge and

discharge responses
Shape 4 (monotonically decreasing profile) is observed primarily after failure events or under strongly asymmetric conditions. In symmetric cells, it often appears immediately following short-circuit episodes, when the morphological structure of the electrode has been irreversibly altered. Its occurrence is therefore associated with post-failure or degradation-dominated regimes rather than with regular cycling behavior.

5.3. CELL-VOLTAGE TRANSIENT (V(t)) CLASSIFICATION FOR MAC MODEL SOLUTIONS

The morphological classification introduced in Section 5.1 was derived exclusively from the inspection of experimental voltage transients. The natural subsequent step consists in verifying whether the same waveform families emerge from the physics-based Metal Anode Charging (MAC) model and, if so, under which parametric conditions.
The objective of this section is therefore to classify the voltage transients generated by numerical solutions of the MAC model according to the same heuristic taxonomy previously established. In this way, a direct correspondence between experimentally observed waveform morphologies and model-predicted electrochemical regimes can be constructed.
To ensure conceptual clarity and to isolate the dominant transport-kinetic and morphochemical mechanisms, the present analysis is restricted to a physically relevant sub-space of the parameter space, defined as detailed below.
First, the exploration is limited to the *periodic regime*, obtained by imposing

$$FC = 0 \quad \text{and} \quad K_{\text{pass}} = 0, \tag{41}$$

thereby eliminating cumulative dendritic growth and passivation effects. Even though the quantitative description of battery failure modes is neglected with this selection, by far the largest fraction of battery cycling datasets can be modelled in this section of the parameter space. Under these assumptions, all the metal deposited during the cathodic semi-period is completely removed during the anodic semi-period, and neither progressive loss of active surface area or passivation can occur. This configuration corresponds to a non-pathological, fully reversible morphological regime, where electrode geometry does not accumulate irreversible distortions over successive cycles. The resulting system dynamics are therefore governed exclusively by ionic transport and intrinsic charge-transfer kinetics, without long-term morphological memory effects. In fact, in the framework of this approximation, morphochemical evolution can be indirectly accounted for by monitoring the variation of transient shape classes over cycling.
Second, the classification search is deliberately constrained to the waveform families identified in Section 5.1. The model exploration does not aim to discover new transient categories, but rather to determine whether the MAC framework is capable of reproducing the four experimentally observed morphological classes (Shapes 1–4) within physically meaningful parameter ranges. This restriction ensures methodological coherence and enables a one-to-one comparison between experimental evidence and theoretical predictions.
Within this controlled setting, the classification of model-generated voltage transients serves a dual purpose. On the one hand, it validates the capability of the MAC model to reproduce the qualitative diversity observed experimentally. On the other hand, it allows the identification of the multidimensional parameter regions associated with each transient morphology, thereby laying the foundation for the parametric mapping developed in the subsequent sections.
By focusing on periodic solutions and on a predefined morphological taxonomy, the present analysis establishes a structured bridge between experimental waveform inspection and physics-based regime identification.

5.3.1 Euristic parameter identification for the symmetric-cell MAC model

Once the four characteristic transient morphologies had been established, the next step consisted in determining whether the symmetric-cell MAC model is capable of reproducing each waveform family within physically meaningful parameter ranges.
Regarding the determination of the different transient morphologies, the modeling approach followed a distinction based on the prevailing charge-transfer mechanism. In the initial phase, Shapes 1, 2, and 3 were identified by fixing the parameter at a typical value for zinc electrodeposition and corrosion processes, where charge transfer is controlled by the electrochemical process. In this regime, the kinetic terms (expressed in eq. 39) play a fundamental role in defining the system's voltage response. Each characteristic morphology was identified by exploring the parameter space within 'physically meaningful' ranges as later better described in section 5.3.3
Conversely, Shape 4 was obtained by imposing the condition $B \approx 0$. This choice represents a formal way to describe a transition in the physical mechanism: charge transfer no longer occurs through an electrochemical reaction at the interface, but via direct electronic conduction.

In this scenario, the temporal dynamics of the cell cease to depend on charge-transfer kinetics and become dominated exclusively by ionic diffusion in the electrolyte (parameter d) and the growth of metallic protrusions at the electrode surface (parameter r_{max}).
Consistent with this interpretation, Shape 4 is observed experimentally almost exclusively after cell failure, confirming that profound structural changes—such as extreme dendritic growth—become the prevailing mechanism controlling the system's response. A representative set of parameters was identified to obtain each of the four characteristic morphological families, as illustrated below. It is important to emphasize that these shapes are not uniquely determined by a single parameter vector; rather, multiple combinations of transport coefficients and kinetic constants can lead to the same characteristic transient profile.

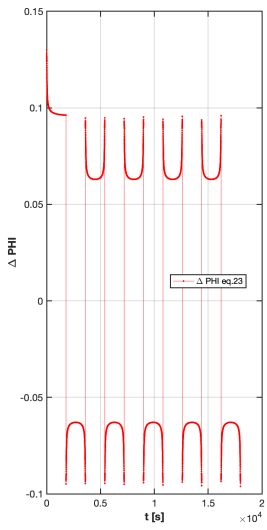

Figure 4: Shape 1

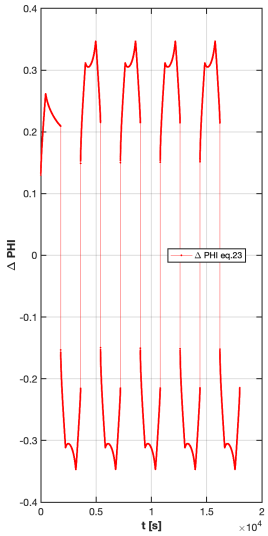

Figure 5: Shape 2

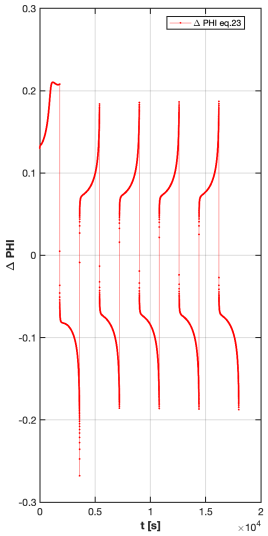

Figure 6: Shape 3

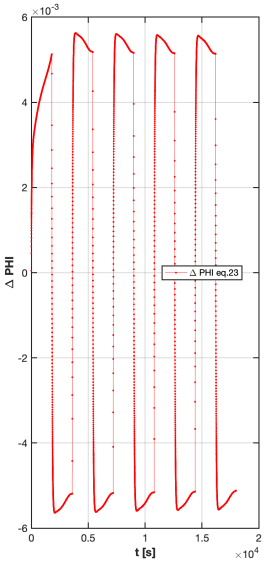

Figure 7: Shape 4

The parameter sets identifying each shape are:
Shape 1: $d = 3 \times 10^{-5}$, $r_{max} = 0.01$, $k_{0,slow} = 9 \times 10^{-7}$, $k_{0,fast} = 1 \times 10^{-6}$, $i_0 = 0.20$, $B = 26$;
Shape 2: $d = 7 \times 10^{-7}$, $r_{max} = 0.03$, $k_{0,slow} = 9 \times 10^{-7}$, $k_{0,fast} = 3.5 \times 10^{-7}$, $i_0 = 0.2$, $B = 26$;
Shape 3: $d = 3 \times 10^{-7}$, $r_{max} = 0.1$, $k_{0,slow} = 9 \times 10^{-7}$, $k_{0,fast} = 5 \times 10^{-6}$, $i_0 = 0.2$, $B = 26$;
Shape 4: $d = 7.53 \times 10^{-6}$, $r_{max} = 0.05$, $k_{0,slow} = 2.4 \times 10^{-7}$, $k_{0,fast} = 2.17 \times 10^{-8}$, $i_0 = 0.2$, $B = 0.001$.

5.3.2 Euristic parameter identification for the full-cell MAC model

An analogous heuristic procedure was applied to the extended MAC model for the full Zn–Ni configuration. In this case, the voltage transient results from the superposition of morphology-driven zinc dynamics and the thermodynamically governed response of the Ni/NiOOH electrode.
The waveforms obtained using the extended full-cell model can be classified according to the same fundamental morphological categories identified for symmetric systems. The modeling effort was specifically directed toward reproducing the waveforms that emerged most consistently from the experimental datasets which has been described in section 5.1.3.
Although the waveforms generated by the full-cell model can be classified according to the same categories established for the symmetric configuration, it is essential to emphasize the pronounced asymmetry observed, in the Ni-Zn systems, between the charge and discharge phases. This asymmetry originates from the intrinsic thermodynamic differences between the charging and discharging curves of the nickel electrode. When these distinct cathodic contributions are superimposed onto the morphology-driven response of the zinc anode, the resulting cell voltage exhibits a marked divergence between the positive and negative semi-periods of the cycle. This behavior is quantitatively evidenced by the parameter sets required to reproduce the observed profiles. Specifically, to obtain Shape 3 during the negative semi-period, the diffusion coefficient (d) must be reduced by three orders of magnitude, while the exchange current density (i_0) must be increased from 0.2 to 2. This significant parametric shift underlines how the coupling of solid-state intercalation thermodynamics with metallic anode dynamics fundamentally alters the system's electrical signature compared to the symmetric case.

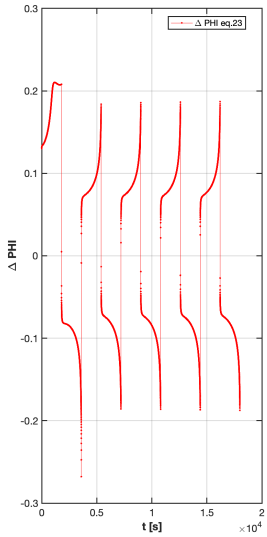

Figure 8: Shape 3 pos. semi-period

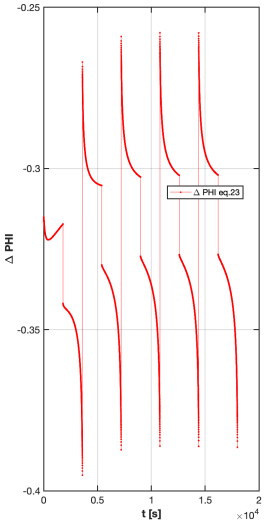

Figure 9: Shape 4 pos. semi-period

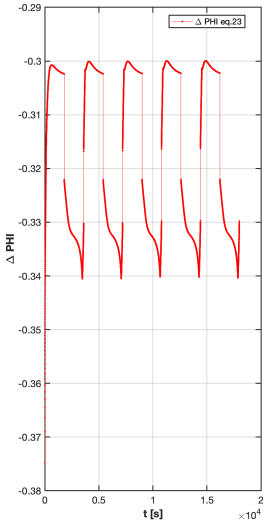

Figure 10: Shape 2 pos. semi-period

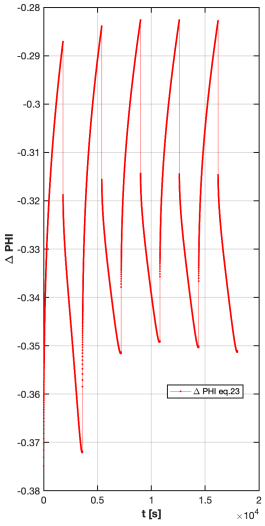

Figure 11: Shape 3 neg. semi-period, 'symmetric behavior'

The sets of parameters identifying each shape are:
Shape 3 positive: $d = 3.2 \times 10^{-5}$, $r_{max} = 0.05$, $k_{0,slow} = 9 \times 10^{-7}$, $k_{0,fast} = 3.5 \times 10^{-7}$, $i_0 = 0.20$, $B = 26$;
Shape 4 positive: $d = 5.7 \times 10^{-8}$, $r_{max} = 0.215$, $k_{0,slow} = 1.5 \times 10^{-9}$, $k_{0,fast} = 6.9 \times 10^{-8}$, $i_0 = 0.2$, $B = 26$;
Shape 2 positive: $d = 9 \times 10^{-7}$, $r_{max} = 0.02$, $k_{0,slow} = 9 \times 10^{-7}$, $k_{0,fast} = 3.5 \times 10^{-7}$, $i_0 = 2$, $B = 26$;
Shape 3 negative: $d = 3.2 \times 10^{-8}$, $r_{max} = 0.05$, $k_{0,slow} = 9 \times 10^{-7}$, $k_{0,fast} = 3.5 \times 10^{-7}$, $i_0 = 2$, $B = 26$.

In is worth noting that, although the principal transient shape classes remain consistent with those observed in symmetric cells, the parameter values required to obtain them differ.
The systematic exploration of the relevant parameter subspace for the full-cell model was focused exclusively on the regions corresponding to Shapes 3 and 4, as these were identified as the most recurrent morphologies in Section 5.1.3. This investigation was conducted using two distinct approaches to characterize the stability of these predominant regimes. First, a single-parameter sensitivity analysis was performed by varying each parameter independently to identify the specific ranges within which the initial morphology is preserved. Subsequently, a global mapping was executed by varying the parameters jointly through a Monte Carlo search, allowing for a comprehensive visualization of the parameter subspace associated with these characteristic full-cell transients.

5.3.3 Single-parameter sensitivity analysis for the symmetric-cell MAC model

Following the heuristic identification of representative parameter sets capable of reproducing each waveform family, a local, single-parameter sensitivity analysis was performed in order to assess the robustness of the corresponding transient morphologies.
To evaluate the sensitivity of the system to the four parameters selected and described in Section 5.3.1, each variable was perturbed within a range of plus or minus one order of magnitude relative to its reference value. This logarithmic variation is physically justified by the inherent uncertainty and the wide range of potential values that electrochemical parameters, such as diffusion coefficients and kinetic constants, can assume depending on the specific electrolyte environment, local concentration gradients, and the evolving state of the electrode surface. From a diagnostic standpoint, this interval allows for a comprehensive exploration of the transition between transport-limited and kinetics-controlled regimes while ensuring the model remains within a physically plausible domain.
The analysis was initiated starting from each of the four principal transient morphologies identified in Section 5.3.2. A one-factor-at-a-time (OFAT) approach was adopted, whereby each parameter was varied individually while keeping the remaining parameters constant.

This methodology enables direct assessment of the relative impact of each parameter on transient evolution and morphological behavior. More precisely referring to **??**, starting from the baseline configuration (black curve), eight progressively increasing values were selected within a right-sided neighborhood of the reference parameter (red curves), and eight progressively decreasing values—logarithmically spaced—were selected within a left-sided neighborhood (blue curves). The corresponding responses are plotted in the panels of **??** to visualize the influence of parameter variations on the waveform. In some cases, the numerical solver failed to converge for parameter values smaller than the baseline configuration; consequently, only the right-sided perturbations (red curves) are reported in those instances.

	d	$\boldsymbol{r_{\max}}$	$\boldsymbol{k_{0,\text{fast}}}$	$\boldsymbol{k_{0,\text{slow}}}$
SHAPE 1	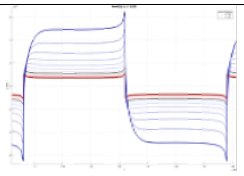	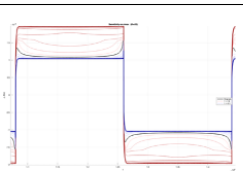	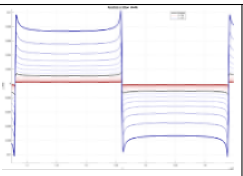	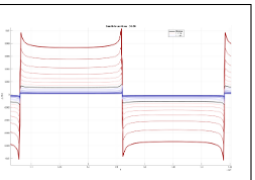
SHAPE 2	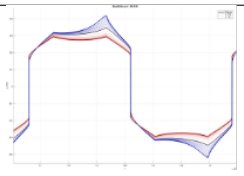	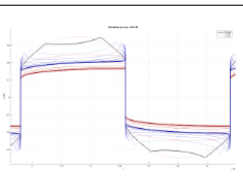	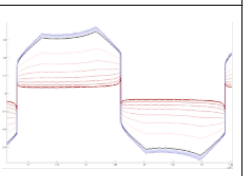	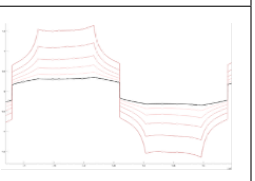
SHAPE 3	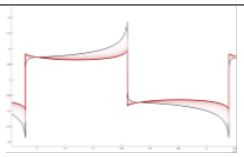	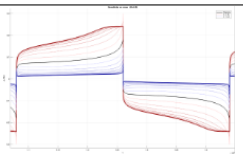	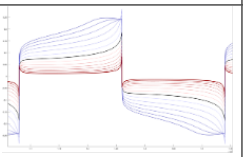	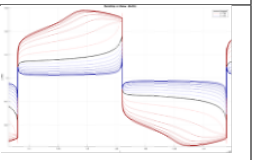
SHAPE 4	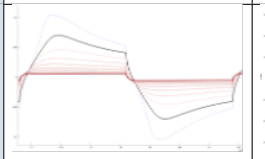	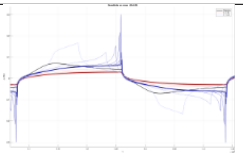	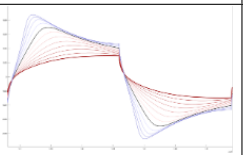	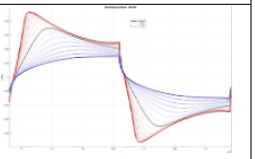

Table 5: Sensitivity analysis for different waveforms (Shapes 1–4) as a function of the parameters d, $r_{\max}$, $k_{0,\text{fast}}$, and $k_{0,\text{slow}}$.

As previously demonstrated by Quarta et al. [11], both d and $r_{\max}$ play a significant role in determining the shape of the voltage transient in a symmetric cell; however, the influence of the kinetic parameters $k_{0,fast}$ and $k_{0,slow}$ has not yet been systematically examined. From these analyses, it was possible to observe that the parameters $k_{0,fast}$ and $k_{0,slow}$ exhibit a significant impact on the morphology of the transient response.

5.3.4 Single-parameter sensitivity analysis for the full-cell MAC model

For the sensitivity analysis of the full cells, the same code was employed, of course, implementing the appropriate boundary conditions. For each simulation, one parameter at a time was varied in order to isolate and assess its individual effect on the symmetry of the response and on the voltage transient profiles associated with shapes 3 and 4. As for the symmetric case, each parameter was perturbed by one order of magnitude in both the positive and negative directions with respect to its reference value.
From **??** it is evident that, by varying the parameter by one order of magnitude, the shapes appear to be stretched or compressed without undergoing significant changes. For a more detailed analysis, see Appendix B.

	d	$r_{\max}$	$k_{0,\text{fast}}$	$k_{0,\text{slow}}$
SHAPE 3	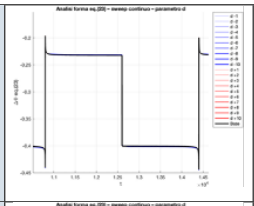	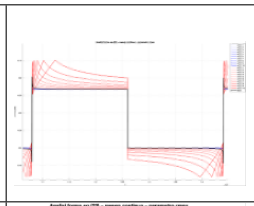	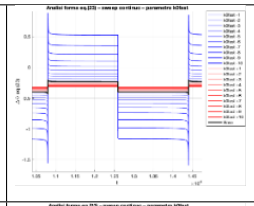	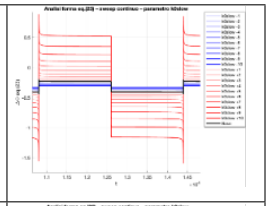
SHAPE 4	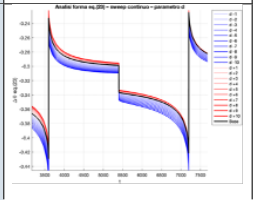	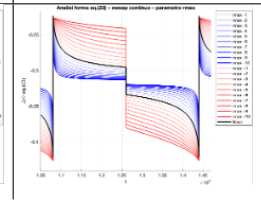	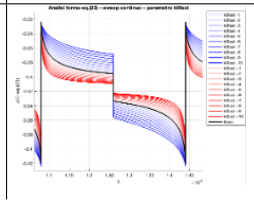	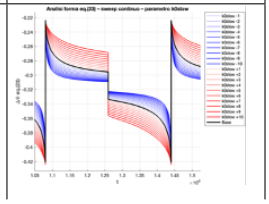

Table 6: Sensitivity analysis for different waveforms (Shapes 3 and 4) as a function of the parameters d, $r_{\max}$, $k_{0,\text{fast}}$, and $k_{0,\text{slow}}$.

5.3.5 Global sensitivity analysis for the symmetric-cell MAC model

To investigate the influence of applied current and electrolyte chemistry on the key physicochemical parameters, a preliminary exploration of the parameter space was first conducted. Specifically, we sought to determine which combinations of model parameters, within the multidimensional parameter space defined in section 5.3.3, yield a given transient voltage profile. The same assumption about the parameters k_{pass} and FC, made in section 5.3, will remain valid, since the primary focus was on the transport and morphological effects.
The three principal parameters, r_{max}, d, and $k_{0,fast}$, were varied within ranges delimited by physical plausibility, while $k_{0,slow}$ was held at a fixed value. This decision is supported by the analysis in Section 5.3.3, which indicates that both $k_{0,fast}$ and $k_{0,slow}$ exert a relatively lower influence on the transient morphology compared to the other two governing parameters. The choice to focus exclusively on $k_{0,fast}$ as a first approach is further justified by the observed "mirrored" behavior between the two kinetic constants; specifically, the sensitivity trends of $k_{0,fast}$ and $k_{0,slow}$ were found to be essentially symmetric (as an increase in one effectively corresponds to a decrease in the other's relative impact). As consequences es, it has been chosen to change only $k_{0,fast}$ as a first approach. For the sake of completeness, additional plots illustrating the system's response as a function of $k_{0,slow}$ are provided in Appendix B.1. It is important to notice that, "shape 4", was not included in the initial investigation, since its occurrence depends explicitly on the value of parameter B, in the parametric study and morphological mapping, Form 4 was examined separately from the other three shapes. The Monte Carlo–based mapping method provided an efficient qualitative approximation of the regions in parameter space associated with each characteristic waveform . It is important to emphasize that the decision to initially restrict the variation to a subset of parameters was a deliberate methodological choice aimed at isolating the dominant transport-kinetic mechanisms, rather than a structural limitation of the mapping algorithm itself. By keeping $k_{0,slow}$ at a fixed reference value during this first stage, the dimensionality of the problem was simplified to highlight the primary contributions of r_{max}, d, and $k_{0,fast}$ While this approach did not involve the systematic variation of $k_{0,slow}$ at the outset—thereby momentarily narrowing the exploration of the full parameter space—it provided a clearer baseline for identifying the fundamental physical regimes.

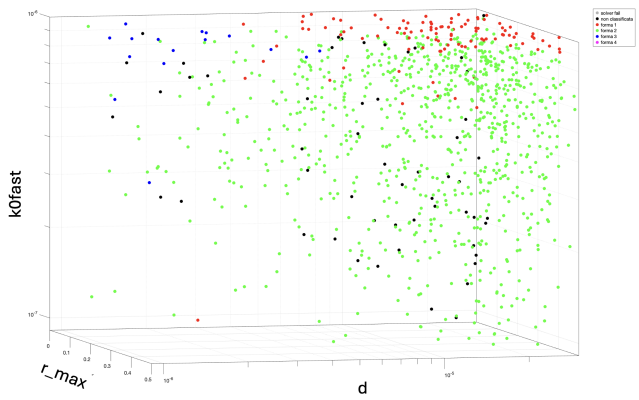

Figure 12: Monte Carlo based mapping.

To obtain a better data representation, a more comprehensive mapping strategy was adopted, account simultaneous for variations of all three principal parameters. In the revised mapping framework, the 3 main waveform families were first identified within the three-dimensional parameter space. The developed code performs a parametric sensitivity and classification analysis around four predefined reference parameter sets of the model. For each reference configuration, it generates multiple perturbed parameter combinations by applying random variations in logarithmic space, in the parameter space defined in section 5.3.3. Each perturbed set is simulated using the MAC model, and the resulting voltage response is categorize based on the approach defined in the section: 5.1.4. The results are then visualized in a three-dimensional logarithmic parameter space, where each point is color-coded according to its classified behavior, thus allowing a clear identification of regime stability and transitions within the explored parameter domain.

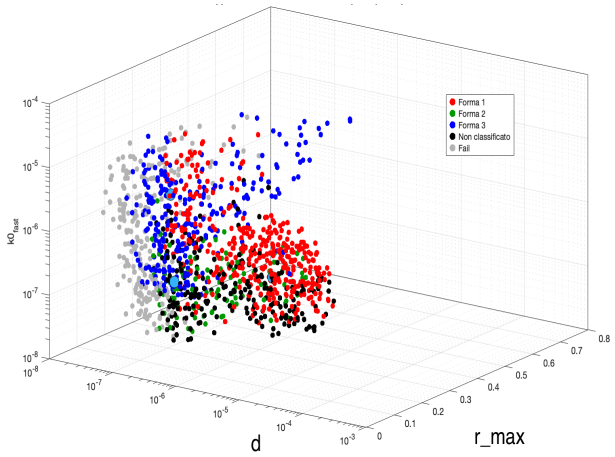

Figure 13: Full three-dimensional logarithmic parameter space mapping of waveform classification

It is important to emphasize that the observed waveform families are influenced by different values of $k_{0,\text{slow}}$, but sice the visualization is inherently three-dimensional, the value of $k_{0,slow}$, although varied at every iteration, cannot be directly represented in the graphical output. Consequently, its individual contribution to the emergence of the different waveform families cannot be unambiguously isolated from the present graphical analysis. A preliminary investigation into the possible effects of the $k_{0,\text{slow}}$ parameter on the waveform shape are reported in Appendix B.1.
By looking at the parametric maps, Shape 1 predominantly occurs at high values of d, corresponding to enhanced mass transport in the bulk phase. A large diffusion coefficient indicates an efficient ionic transport process. From a physical standpoint, such behavior may arise from modifications in electrolyte chemistry or in the solid electrolyte interphase (SEI), which can promote improved ion solvation or lead to the formation of reaction products that facilitate ionic mobility [12].
In contrast, Shapes 2 and 3 prevail in regions characterized by low values of d, indicative of diffusion-limited conditions. In this regime, slower mass transport hinders homogeneous ionic redistribution, thereby favoring alternative morphological evolutions.
Furthermore, both Shape 1 and Shape 3 are associated with elevated values of $k_{0,\text{fast}}$. This kinetic parameter quantifies the rates of electrodeposition and stripping at the most reactive surface regions, namely the apices of hemispherical protrusions (i.e., dendrite tips). High values of $k_{0,\text{fast}}$ imply strong electric field intensification and a concomitant increase in local tip current density, thus accelerating interfacial growth dynamics.

Symmetric model	r_{max}	d	K_{0fast}
SHAPE 1	Medium-small	high	Medium-high
SHAPE 2	small	small	small
SHAPE 3	Small-high	small	high

Table 7: Summary of symmetric model parameters for different shapes.

To investigate Shape 4, the same computational framework was employed, with the only modification being the parameter ($B \approx 0$) as detailed in Section 5.3.1. Consistently with the previous procedure, sets of parameters

were generated in the neighborhood of the reference (base) configuration and subsequently classified according to the established criteria.
As shown by the resulting parameter maps as shown in 14, Shape 4 exhibits a pronounced sensitivity to perturbations. Even for relatively small variations (on the order of 30%), the system rarely preserves the characteristic features associated with this shape. This behavior indicates that the parameter combination corresponding to Shape 4 lies in a highly localized and isolated region of the parameter space, suggesting limited structural robustness with respect to parametric perturbations.

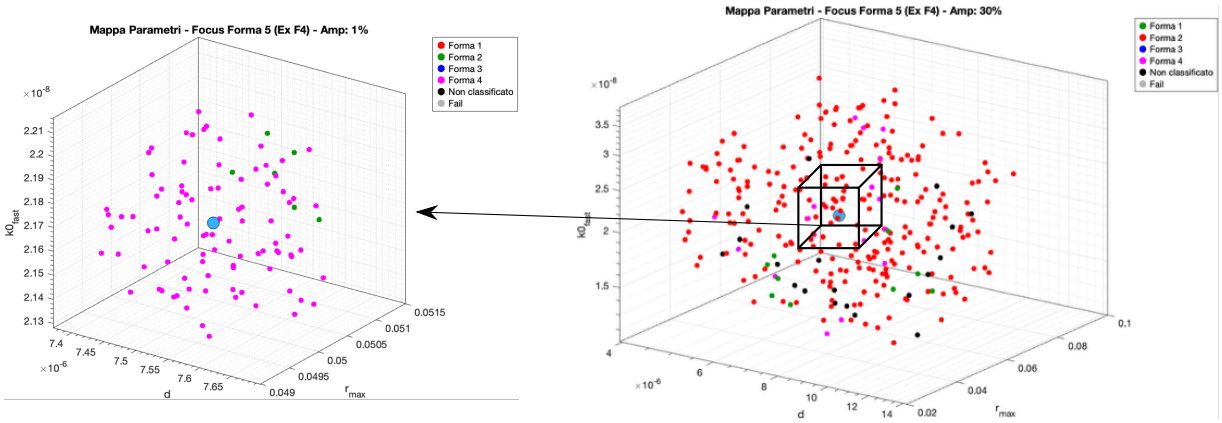

Figure 14: Parameter map with zoomed region close to shape 4.

5.3.6 Global sensitivity analysis for the full-cell MAC model

As characteristic of the full-cell case, separate morphological classifications are needed for the charging and discharging half-cycles. To account for this behavior, the Monte Carlo mapping procedure was reformulated to analyze the two semi-periods separately. To account for the intrinsic electrochemical asymmetry of the system, the classification was performed independently for each semi-period. This approach yielded two distinct three-dimensional Monte Carlo maps characterizing the morphological distribution during positive and negative polarization, respectively. This approach allows direct visualization of how the same parameter combination produces different transient shapes depending on the current direction, thereby quantitatively capturing the intrinsic electrochemical asymmetry of the Zn–Ni system.

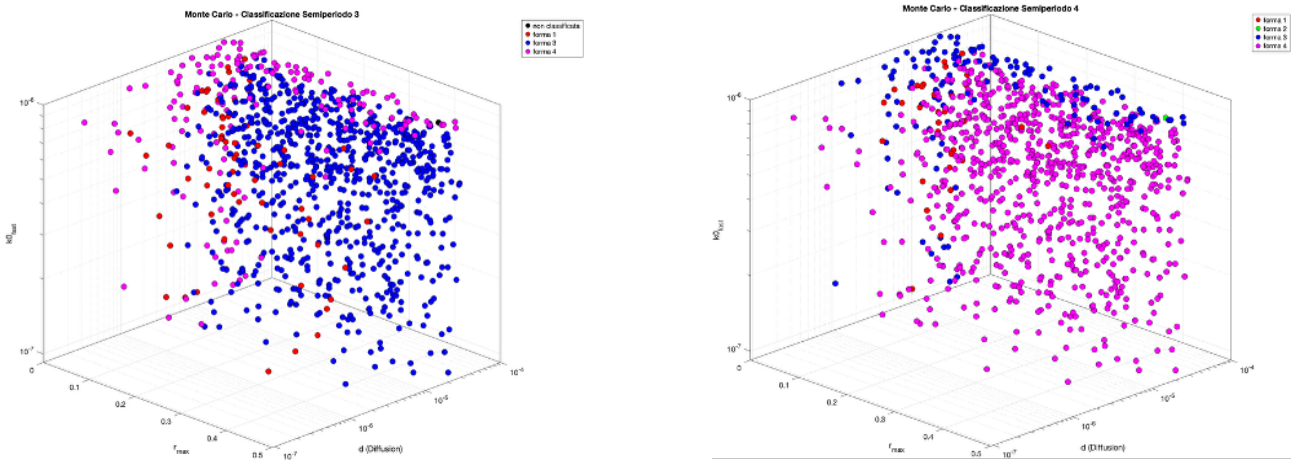

Figure 15: Negative and positive semiperiod Monte Carlo based mapping.

Similarly to the symmetric configuration, following an initial Monte Carlo mapping, a more comprehensive strategy was adopted to provide a more effective representation of the entire dataset. In this case, for the reason described in section 5.3.2, the parameter space mapping shown in Fig 16, was constructed starting from the set of parameters which identify shape 3 and 4. The mapping was also conducted by distinguishing between the negative and positive semi-periods. The resulting mapping, shown in Fig 16, clearly highlights the intrinsic asymmetry of the full model, which is reflected both in the distribution of the stability regions and in the different extent of the parameter areas associated with the two dominant forms in their respective semi-periods.

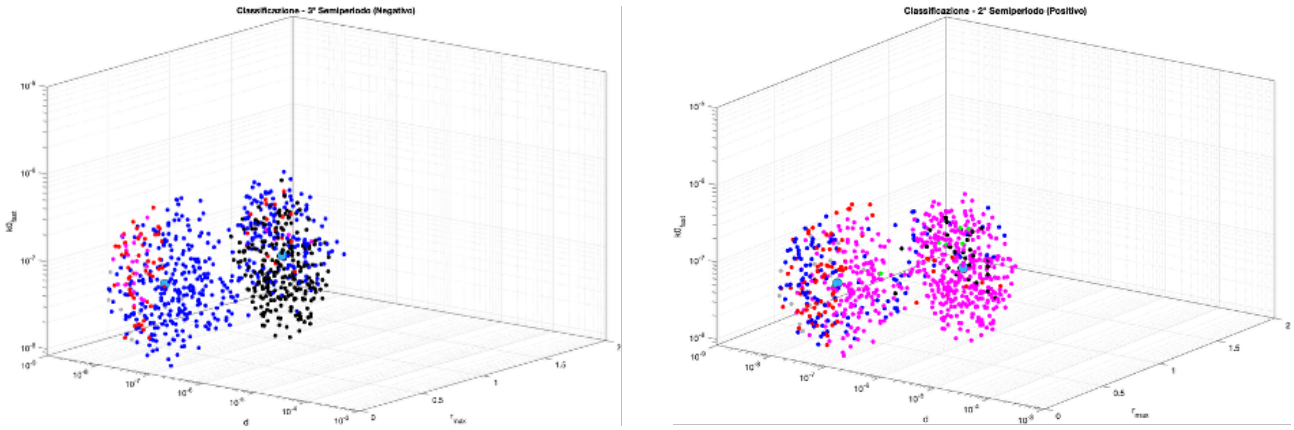

Figure 16: Positive and negative semiperiods: shape evolution around 'shape 3' and 'shape 4'

Full model	Semi period	r_{max}	d	K_{0fast}
SHAPE 3	positive	small	small	small
SHAPE 4	positive	small	medium-high	small
SHAPE 3	negative	small	medium-high	small
SHAPE 4	negative	small	small	small

Table 8: Full model parameter comparison for different shapes and polarities.

5.3.7 Comparison between symmetric and full model classification

A comparison between the global sensitivity analysis of the full-cell and symmetric-cell models reveals a significant redistribution of the stability regions for the characteristic waveforms. In the symmetric configuration, Shape 1 was a prevalent feature occurring predominantly at high diffusion levels; however, in the full-cell model, its occurrence is markedly restricted to low diffusion values and localized to a very small number of points, which is consistent with the experimental absence of Shape 1 in full-cell datasets. A more dramatic transformation is observed for Shape 4. While in the symmetric model Shape 4 was confined to a highly localized and isolated region of the parameter space, indicating limited structural robustness and low sensitivity to perturbations, it becomes a dominant configuration in the full-cell framework. In the full-cell model, Shape 4 is extensively present and prevails throughout the regions associated with high diffusion, reflecting how the intrinsic electrochemical asymmetry fundamentally expands the parameter space associated with this specific morphological regime.

5.4. ELECTROCHEMICAL MATERIALS-SCIENCE CONCLUSIONS OF MAC-MODEL BASED ANALYSIS

The morphology-based classification and the parameter-space exploration developed in the previous sections provide a structured framework for interpreting the electrochemical behavior of the investigated systems. In this section, the results are discussed from a materials-science perspective, focusing on how electrolyte composition and operating conditions influence the distribution of voltage transient shapes.
Rather than relying exclusively on integral metrics such as time-to-failure, the present analysis interprets cell behavior through the evolution and prevalence of the identified waveform families. The transient morphology is therefore used as a diagnostic descriptor linking experimental observations to underlying electrochemical regimes.

5.4.1 Symmetric Zn–Zn cells with aqueous electrolyte: effect of additives on Potential Transient Shape

The morphology-based classification and the parameter-space exploration developed in the previous sections provides a structured framework for interpreting the electrochemical behavior of the investigated systems. In this section, the shape and parameter-region identification results are discussed from a materials-science

perspective, focusing on how electrolyte composition, electrode treatment and operating conditions influence the distribution of voltage transient shapes.
Rather than relying exclusively on integral metrics such as time-to-failure, the present analysis interprets cell behavior through the evolution and prevalence of the identified waveform families. The transient morphology is therefore used as a diagnostic descriptor linking experimental observations to underlying electrochemical regimes.
The first set of conclusions concerns symmetric Zn–Zn cells operated in near-neutral aqueous electrolyte with different zwitterionic additives. The automated classification revealed that each additive is associated with a characteristic distribution of transient morphologies and with a specific evolution pattern during cycling.
The first dataset analysed comprised symmetric cells containing three different additives: NBSD-195, NBSD-201, and NBSD-25. All cells consistently exhibited the same characteristic transient response, identified as Shape 1. Cells containing NDSB 201 and NDSB 257, exhibit a pronounced presence of shape 3 voltage transients which is characterized by a monotonic increase in voltage within a galvanostatic semi-period. In NDSB 201 cells, this morphology typically emerges shortly before short circuit, whereas in high-current NDSB 257 systems it is observed from the early stages of cycling. This change in waveform from Shape 1 to Shape 3 can be justified as a progressive roughening of the surface. The accumulation of "dead metal" or irreversible changes in the electrode morphology can alter the local electric field. If these alterations lead to surface saturation or degradation-induced passivation, the voltage profile departs from the regulated shape (Shape 1) and evolves toward a continuously increasing behavior (Shape 3). This transition signifies a shift from the enhanced mass transport regime characterized by high diffusion coefficients, which is typical of Shape 1, toward the diffusion-limited conditions associated with significantly lower values characteristic of Shape 3.
Experimental observations reveal that the average duration preceding short-circuit events is minimized for additive NDSB 195 and maximized for NDSB 257. The superior interfacial affinity of NDSB 257, relative to NDSB 195, may be attributed to structural disparities that facilitate stronger surface interactions within highly concentrated (4 M) aqueous environments. Specifically, the NDSB 257 molecule features an aromatic moiety that confers higher molecular polarizability. Consequently, these molecules preferentially stabilize in regions of intensified electric fields, such as dendrite tips, characterized by a smaller radius of curvature. By selectively adsorbing onto these protruding sites, the additive increases local charge transfer resistance and suppresses the local current density (j_{tip}). This mechanism redistributes the zinc ion flux toward planar regions, promoting a more uniform surface morphology and effectively decelerating dendritic outgrowth. Furthermore, the partial hydrophobic character associated with the aromatic group may reduce full bulk solvation and thermodynamically favour interfacial accumulation. Consequently, NDSB 257 is likely to form a more persistent interfacial layer, which may modulate Zn^{2+} flux and contribute to more homogeneous nucleation and improved interfacial stability.
The primary failure mechanism observed in all cells is short circuiting, which arises from morphological changes at the electrode surface, particularly from the outgrowth of metallic protrusions[8]. As these structures progressively extend, they may eventually penetrate the separator and establish contact with the opposing electrode. This creates a conductive potential bridge between the electrodes, leading to a sharp drop in the measured cell potential to significantly lower values. Under these conditions, the cell effectively behaves as a simple resistive element.
However, the phenomenon observed here does not correspond to a permanent short circuit in the strict sense, but rather to what has been described in the literature as a labile short-circuit condition [4]. Because the metallic contact is mechanically fragile and subjected to high local current densities, it may partially dissolve or fracture under operation. As a result, the electrical connection can be intermittently interrupted, allowing the cell to resume operation [11].
Following such events, the cell consistently restarts with voltage transients that are noisy and poorly defined, irrespective of the additive employed. This behavior can be attributed to the severely altered electrode morphology. The surface becomes highly irregular, leading to pronounced asymmetries between the two electrodes. These morphological instabilities give rise to non-uniform current distribution and irregular transient responses in subsequent cycling, leading to what has been called in the shpe vs semiperiods graph, 'unclassified shape'.
Some cells with NDSB 257 (and to a lesser extent NDSB 201), exhibiting clear passivation phenomena toward the end of measurements, which may be due to an excessive surface adsorption of the additive at the electrode interface, reducing the active surface area and increase current localization, so care must be taken regarding its concentration; excessive adsorption on the active sites may promote electrode passivation, thus limiting the overall electrochemical stability.
An analysis of the experiments conducted across varying current densities (0.7, 1, and 5 mA cm^{-2}) demonstrates that increasing the applied load leads to a consistent reduction in the time-to-failure for the symmetric Zn‖Zn cells. This trend is primarily driven by the higher overpotentials associated with elevated current densities, which lower the energetic barrier for metal nucleation and accelerate zinc deposition. In accordance with the Butler–Volmer relationship, where even marginal fluctuations in overpotential trigger exponential shifts in local current density, minor surface perturbations are significantly amplified. Specifically, the electric field is

intensified at the tip of surface protrusions due to the reduced local radius of curvature. This field enhancement promotes localized surges in current density, facilitating preferential Zn^{2+} consumption and rapid deposition at these sites. As a result, dendritic outgrowth is accelerated under high current density conditions., leading to premature cell failure.
In addition, at high current densities, the consumption of Zn^{2+} near the electrode surface increases substantially, leading to a decrease in the local ion concentration, increasing local resistivity The resulting concentration gradients increasing the voltage ohmic loss, further amplifying deposition at protrusions where the resistance is lower, promoting morphological instability.
Moreover, the effectiveness of interfacial additives may decrease at high current densities. The intensified interfacial electric field can facilitate additive desorption or reduce their surface residence time, thereby diminishing their ability to regulate Zn deposition and suppress dendrite formation.

Molecules structure	**Additive's name**	**Time to failure (h), 5 mA/cm^2**	**Time to failure (h), 1 mA/cm^2**	**Time to failure (h), 0.7 mA/cm^2**
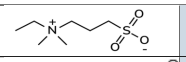	NDSB-195	39.4 ± 3.4	66 ± 14	126.6 ± 16
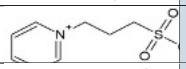	NDSB-201	78 ± 15	208 ± 77	231.9 ± 13.5
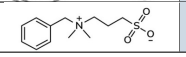	NDSB-257	104.6 ± 14.8	305.6 ± 113.4	317.3 ± 42

Table 9: Time to failure comparison for different additives.

5.4.2 Symmetric Zn–Zn cells with aqueous electrolyte: effect of metal foil cutting method

To further consolidate and stress-test the shape-recognition algorithm, additional symmetric Zn–Zn cells were analyzed [Elisa data reference]. In this case, all cells were operated under identical current density and experimental conditions, but they differed in the electrode fabrication method: mechanically punched, shielded punched, and laser-cut electrodes. For each fabrication technique, 10 replicates were produced (10 cells per method), and each cell was analysed using the automated shape-recognition procedure. Across all 30 cells, a common behavior was observed. The characteristic profile was consistently identified as Shape 3, corresponding to a monotonic increasing voltage curve during the half-cycle. Following short-circuit events, the voltage transients generally resumed with an irregular variant of Shape 4, typically characterized by pronounced voltage spikes. These spikes are most likely associated with the formation of ZnO layers on the surfaces of both electrodes. Such layers act as an insulating medium, effectively behaving as a dielectric between two capacitive elements. As a result, charge accumulation occurs and the cell exhibits the behavior of an RC circuit. After this irregular transient, the voltage profile often returned to a regular monotonic increase (Shape 3). This sequence was observed repeatedly throughout the lifetime of the cells. Moreover, all these cells exhibited an asymmetric voltage trends after failure in which Shapes 3 and 4 alternated mainly with Shape 1 and "unclassified" profiles. This asymmetry was particularly pronounced in laser-cut cells, suggesting a higher degree of electrochemical instability associated with this fabrication method. The alternation between Shape 3 and Shape 4 indicates a regime of high electrochemical instability typically observed following cell failure, signifying that the two electrodes are no longer operating under equivalent morphological or kinetic regimes. Shape 3 is associated with diffusion-limited conditions characterized by low values of the diffusion coefficient d and progressive surface roughening. Conversely, Shape 4 emerges when charge-transfer kinetics are negligible, specifically when $B \approx 0$, leaving the system dynamics to be governed by mass transport and the growth of metallic protrusions r_{max}. Physically, this repeating sequence represents a labile short-circuit condition, where fragile dendritic contacts intermittently establish and break, causing the voltage to oscillate between a resistive short-circuit response and an unstable monotonic increase.
Regarding the number of cycles before short-circuit, no significant difference was observed among the three cutting methods, despite the expectation that laser-cut cells would exhibit a longer cycle life due to their superior precision and reduced edge deformation. This suggests that the laser cutting process introduces specific detrimental effects in zinc-based cells, in this specific case, due to the presence of machining tabs, to prevent detachment of the disc cut off from a foil, that resulted in current-line concentration effects. These metallic protrusions result in preferential nucleation and corrosion sites.

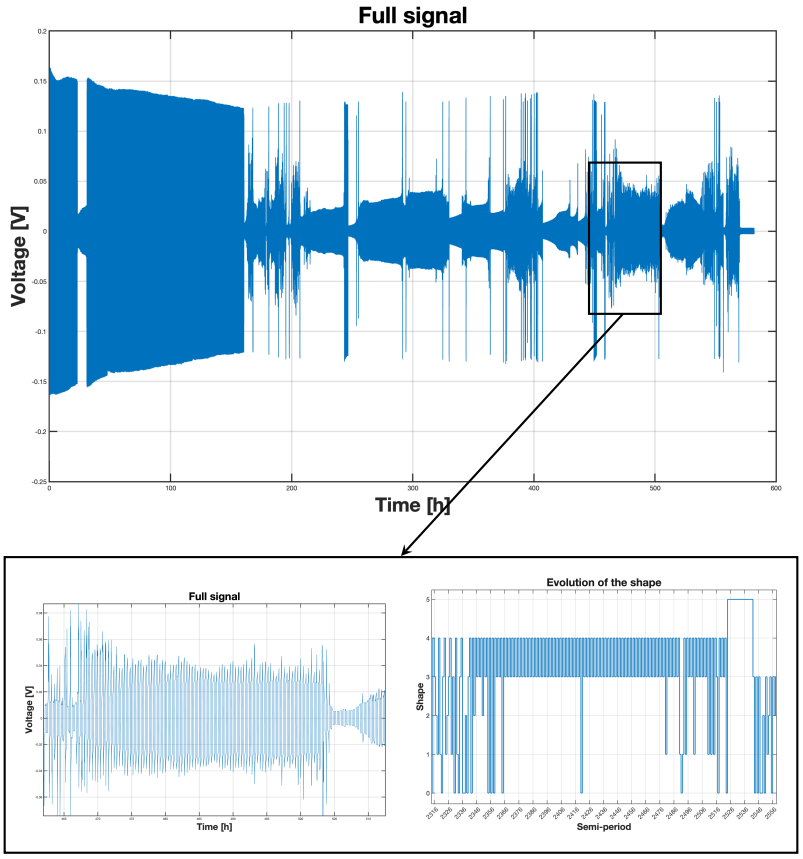

Figure 17: Zoomed-in detail and waveform classification.

5.4.3 Symmetric Zn–Zn cells with DES electrolyte

The analysis of potential transient morphologies was also applied to symmetric Zn–Zn cells employing the deep eutectic solvent (DES) electrolytes discussed in Section 5.1.3.3. Compared to aqueous $ZnSO_4$ electrolytes, DES formulations introduce significant modifications in physicochemical properties, including increased viscosity, altered Zn^{2+} solvation structure, and modified interfacial double-layer characteristics. Use of DES electrolytes results in notably improved cyclability of Zn/Zn symmetric cells, as shown in the appendix, which can be attributed to higher morphological stability. Regarding the transient classification, Shape 3 is the predominant morphology observed across all cells utilizing DES electrolytes, while Shape 1 appears only in the specific and limited case of cells containing the TBAB additive. This distribution is physically consistent with the medium properties; first, the higher viscosity of the DES medium lowers the effective diffusion coefficient of Zn^{2+} ions, which is consistent with the predominant occurrence of Shape 3 profiles in the transient classification. Although reduced ionic mobility increases polarization at elevated current densities, it simultaneously suppresses rapid localized ion depletion near surface protrusions, thereby limiting the amplification of tip-growth instabilities.
Second, the solvation structure of Zn^{2+} in $ZnSO_4$:EG systems differs significantly from that in purely aqueous environments. The presence of ethylene glycol modifies the primary solvation shell and alters the coordination environment of zinc ions. This change can promote more homogeneous nucleation and reduce preferential growth at high-field regions, contributing to a smoother spatial distribution of deposition.
Third, DES environments may favor the formation of more uniform interfacial layers at the zinc surface. Such interfacial regulation mitigates local electric-field intensification and reduces current density localization, further stabilizing the morphological evolution of the electrode. This behavior is reflected in the markedly extended cycling stability of the cells relative to aqueous systems.
Passivation signatures were detected only after extended cycling durations, indicating a gradual surface evolution process rather than abrupt morphological failure.

Effect of DESEG 50%. The DESEG 50% formulation represents a partially diluted DES system. In this case Shape 3 remained dominant during early cycling, and in general, present a lower time to failure (cells failed after few cycles). The reduced viscosity compared to the pure DES increases Zn^{2+} mobility, partially restoring transport characteristics closer to aqueous systems. Physically, this creates a trade-off: (i) Improved

mass transport relative to pure DES, (ii) slightly increased susceptibility to localized deposition instabilities. In summary, the DES electrolyte systems occupy a distinct electrochemical regime characterized by slower but more spatially uniform Zn deposition. The morphology-based classification confirms that these systems provide enhanced structural stability of the zinc electrode, with transient waveform evolution consistent with suppressed morphological amplification compared to conventional aqueous electrolytes.

Effect of TBAB Addition. The incorporation of TBAB into aqueous-based electrolytes, introduces bulky organic cations that can adsorb at the zinc surface. From a physical perspective, TBAB may influence morphology through: (i) surface adsorption and partial blocking of active sites, (ii) modification of the electric double layer, (iii) local alteration of ion flux distribution.
All cells are characterized by an alternating occurrence of Shape 1 and Shape 3 morphologies. This asymmetric behavior may be attributed to a non-uniform distribution of additives across the surfaces of the two electrodes, which significantly modifies the local kinetics of deposition and passivation. These variations fundamentally alter the diffusivity at the two electrode interfaces: in one case, enhanced mass transport supports the regulated transient typical of Shape 1, whereas in the other, a reduction in the effective diffusion coefficient leads to the unstable monotonic increase characteristic of Shape 3.

Physical Effects: AQ vs. DESEG Electrolytes

This section compares the electrochemical behavior of cells employing standard aqueous $ZnSO_4$ electrolytes (detailed in Section 5.1.3.1) with those utilizing the DESEG medium, a deep eutectic solvent (DES) described in Section 5.1.3.3. This comparison is fundamental to evaluate how the solvent nature—specifically the transition from a reactive aqueous environment to a highly viscous DES—modulates the competition between ion transport and parasitic degradation.
Analysis of the voltage transients in the aqueous $ZnSO_4$ system without additives shows a predominant occurrence of Shape 1. From a parameter standpoint, Shape 1 is associated with high values of the effective diffusion coefficient d, which supports a regulated growth regime. However, in the aqueous environment, all tested cells eventually exhibit a clear transition toward passivation by the end of the measurement. This is primarily due to the high reactivity of water, which promotes collateral phenomena such as the hydrogen evolution reaction (HER) and the subsequent accumulation of insulating by-products.
In contrast, the DESEG system predominantly exhibits Shape 3 profiles throughout cycling which is physically consistent with the lower diffusion coefficients d characteristic of the DES medium, where high viscosity limits ionic mobility. Despite the lower diffusivity, the DESEG electrolyte effectively suppresses the parasitic reactions observed in the aqueous case. By reducing the availability of free water at the interface, the DESEG formulation limits the formation of passivation layers, thereby providing a more stable environment for long-term cycling compared to the additive-free aqueous $ZnSO_4$ system.

5.4.4 Full-cells with Zn anode and different cathodes

The following subsections discuss the influence of each cathode on the distribution of transient morphologies, on the persistence of periodic behavior, and on the transition toward monotonic or degradation-associated profiles.

5.4.5 hot pressed and blade coated cells

As Clearly evidenced, and in agreement with the findings reported in [3], cells featuring zinc electrodes fabricated via the blade-coating technique exhibit a significantly extended cycle life compared to those produced by the hot-pressing method. Both cells are characterized by the predominance of Form 3 as the defining transient morphology. However, the blade-coated cell displays a markedly more pronounced asymmetry between the charge and discharge phases. This behavior may be attributed to the influence of zinc electrode thickness on the transient profile[55]. As discussed in [6], thinner electrode architectures promote faster and more homogeneous ionic transport, as the electrolyte is able to penetrate uniformale throughout the entire electrode volume. Such enhanced ionic accessibility can lead to more distinct kinetic differences between charge and discharge processes, thereby amplifying the observed asymmetry in the transient response. This results in a more uniform surface reduction process. Consequently, the ZnO-to-metallic Zn conversion proceeds in a more consistent and spatially homogeneous manner. In contrast, cells fabricated via hot pressing exhibit an almost symmetric voltage profile. In these experiments, a depth of discharge (DOD) of 10% was imposed. Operating within such a narrow window results in nearly specular charge and discharge processes, as the cell remains far from the thermodynamic and kinetic limits associated with full discharge. As can be observed from the waveform mapping analysis, the prevailing behavior throughout most of the cell lifetime corresponds exclusively to Shape 3.However, toward the end of life, an increasing asymmetry between charge and discharge becomes evident in the hot pressed cells. In

particular, the charge curve evolves toward Shape 2, which is characterized by the appearance of a pronounced maximum, as shown in Fig 10. This morphology is associated with significantly higher values of the kinetic parameter $k_{0,fast}$ compared to other shapes. Physically, elevated $k_{0,fast}$ values represent an acceleration of localized electrodeposition at the tips of surface protrusions or dendrites, driven by the intensification of the electric field in those regions. The emergence of this kinetic regime is highly consistent with the end-of-life phase of the cell, where accumulated morphological instabilities and the growth of aggressive dendritic structures lead to high local current densities and imminent failure.

5.4.6 Zn Anode – TQC Cathode

The electrochemical investigation of full cells utilizing TQC cathodes revealed significant differences in stability compared to their symmetric counterparts. Although these systems initially displayed stable cycling, the analysis of voltage transients confirms that the transition to a full-cell configuration leads to an overall degradation of performance metrics. The automated classification algorithm identified a persistent dominance of Shape 3 across both charge and discharge semi-periods, indicating that the system remains primarily governed by transport-limited regimes. This symmetry in waveform morphology suggests that the complex interplay between zinc electrodeposition at the anode and the redox dynamics of the TQC cathode favors a monotonic voltage evolution. However, the observed degradation pathways demonstrate that the coupling of these two electrodes introduces additional instabilities not present in symmetric Zn/Zn studies. Even under moderate current densities, the progressive evolution of the transients towards increasingly polarized Shape 3 profiles suggests that the TQC cathode effectively modulates the cell's potential response but cannot fully mitigate the morphological memory effects of the zinc anode, eventually leading to a more rapid decline in cycling efficiency.

5.4.7 Zn Anode: CMC-Based Cathode

The investigation of full cells employing CMC-based electrodes demonstrates a significant deviation from the electrochemical stability typically observed in symmetric configurations. While these cells show a consistent cycling response in the early stages, characterized by Shape 3 during both charge and discharge, the transition to a full-cell setup is accompanied by an accelerated onset of degradation mechanisms.
The automated transient analysis confirms that Shape 3 remains the dominant profile throughout the entire operational life of the cell, across both charge and discharge semi-periods. In particular, as observed in experiment Esp-4, under a current density of 1.5 mA and a specific capacity of 5.3 mAh cm^{-2} for the Zn foil, the cells reached a premature end-of-life after approximately 20 cycles due to short-circuiting. This performance gap, compared to symmetric Zn/Zn models, indicates that while CMC-related formulations influence the overall potential profile, they provide insufficient stabilization against the dendritic growth and structural instabilities inherent to the zinc anode in a complete cell environment

5.4.8 cells with DES electrolyte in full cell configuration

The morphology-based analysis employing deep eutectic solvent (DES) electrolytes was extended to full-cell configurations. Based on the experimental datasets, these systems utilized a TQC cathode coupled with a zinc foil anode. Two distinct electrolyte formulations were investigated: a concentrated $ZnSO_4$:EG 2 M system and a DESEG 50% version, the latter being a partially diluted DES where the addition of water reduces viscosity and increases Zn^{2+} mobility.
The voltage transients for these cells consistently exhibited a "symmetric" Shape 3 profile, appearing with high regularity in both positive and negative semi-periods. According to the MAC model parameter mapping, this specific configuration is characterized by low diffusion coefficients (d) but high exchange current densities (i_0) as shown in Fig 8.
This combination provides a robust physical explanation for the observed stability that previously seemed counterintuitive. While the low d value (due to high DES viscosity) induces the monotonic potential increase typical of Shape 3, the high i_0 ensures that the interfacial kinetics remain fast and balanced. This high exchange current density effectively "recovers" the symmetry of the transients even in a full-cell setup, mitigating the amplification of tip-growth instabilities by promoting a more uniform reaction rate across the electrode surface. Consequently, the $ZnSO_4$:EG 2 M formulation provides a stable electrochemical environment where the interplay between transport constraints and fast kinetics delays the onset of dendritic failure.
In contrast, cells incorporating TBAB as an additive displayed a markedly different behavior, which appears to disrupt this kinetic equilibrium. In these systems, the voltage profile deviates from the regular Shape 3 pattern shortly before failure, transitioning toward a degenerate form with a significantly reduced number of semi-periods. This suggests that in the specific context of DES-based full cells, TBAB may induce current localization or non-uniform surface adsorption that compromises the stabilizing effect of the high i_0 regime, leading to premature short-circuiting.

Overall, the comparison between DESEG 2 M and DESEG 50% highlights a clear trade-off between transport efficiency and morphological stability. The morphology-based transient classification thus captures how the electrolyte concentration and the balance between d and i_0 directly modulate the electrochemical stability of the TQC-Zn system.

6. Conclusions

This thesis has developed a general unified physics-based and data-driven framework for the interpretation of voltage transients in batteries with metal anodes and intercalation cathodes. Cathode modelling is based on the $Ni(OH)_2/NiOOH$ case, but the formalism adopted can accomodate any conversion cathode chemistry. The approach has been validated with a wide range of experimental cases, spanning symmetric Zn/Zn cells with a range of aqueous without and with additives and non aqueous electrolytes to full cells with Zn anodes and Ni as well as organics cathodes. By moving beyond conventional integral descriptors such as time-to-failure, this work has demonstrated that the morphology of galvanostatic voltage waveforms constitutes a physically meaningful diagnostic observable, capable of encoding degradation mechanisms of conversion metal electrodes jointly with electrokinetics and mass-transport.

Within the symmetric cell configuration, the Metal Anode Charging (MAC) model provided the theoretical backbone for linking metal shape changes - including dendritic growth and passivation - and cell potential response to galvanostatic dicharge/charge cycles, synergising with ionic transport, interfacial kinetics and internal resustance evolution into a coherent mathematical structure. The systematic classification of voltage semi-periods into four fundamental morphological families established a regime-based interpretation strategy, replacing pointwise parameter fitting with the identification of admissible parameter hypervolumes. The implementation of an automated MATLAB recognition algorithm enabled high-throughput analysis of large experimental datasets, revealing statistically robust correlations among waveform morphology, additive chemistry, fabrication method, and applied current density.

The extension of the framework to the full Zn–Ni cell represented a conceptual and mathematical advancement. By incorporating a thermodynamic description of the $Ni(OH)_2//NiOOH$ cathode based on a modified version of the two-parameter Margules formalism, able to account for out-of-equilibrium conditions, the system evolved from a tool for the study of laboratory cells dedicated to metal anode studies, to a general platform for the rationalization of the behaviour of full batteries featuring a metal anode and an intercalation cathode. Despite the intrinsic asymmetry of the full cell, the same morphological classification logic remained applicable, confirming the generality of the regime-based approach.

Across all investigated configurations, the results consistently show that voltage transient morphology is not a secondary or incidental feature of galvanostatic cycling, but rather a structured macroscopic manifestation of internal physico-chemical regimes. Monotonic profiles, curvature reversals, and single-minimum responses correspond to distinct balances between diffusion, charge-transfer kinetics, surface growth, and thermodynamic driving forces. The classification framework therefore acts as a statistical and conceptual bridge between raw electrical testing data and the underlying material evolution.

From a broader perspective, this work contributes to the methodological transition from parameter-centric modeling toward behavior-centric diagnostics in electrochemical energy storage. By emphasizing waveform morphology as a regime indicator, the proposed framework enhances robustness against structural non-uniqueness in inverse problems and provides a scalable strategy for monitoring degradation pathways in next-generation aqueous zinc batteries. Future developments may integrate this physically grounded classification approach with advanced machine learning techniques, enabling real-time adaptive diagnostics and predictive maintenance strategies. In this direction, the combination of first-principles modeling and automated pattern recognition represents a promising pathway toward intelligent, self-diagnostic energy storage systems. Future studies could also investigate the influence of parameters that were kept fixed in the present work, such as the exchange current densities, and passivation rate constants, in order to assess their role in triggering transitions between morphological regimes.

In conclusion, the present study establishes voltage waveform morphology as a rigorous, generalizable, and physically interpretable descriptor of electrochemical regimes, offering both theoretical insight and practical diagnostic tools for the advancement of zinc-based battery technologies.

References

[1] Francesca Rossi, Lucia Mancini, Ivonne Sgura, Marco Boniardi, Andrea Casaroli, Alexander Peter Kao, and Benedetto Bozzini. Insight into the cycling behaviour of metal anodes, enabled by X-ray tomography and mathematical modelling. *ChemElectroChem*, 9(9):e202101537, 2022.

[2] Benedetto Bozzini, Elisa Emanuele, Jacopo Strada, and Ivonne Sgura. Mathematical modelling and parameter classification enable understanding of dynamic shape-change issues adversely affecting high energy-density battery metal anodes. *Appl. Eng. Sci.*, 13:100125, 2023.

[3] Elisa Emanuele, Lucia Mancini, Seyedamin Razaghi, Rožle Repič, Maya Kobchenko, and Benedetto Bozzini. Architecture-driven design of ZnO@C anodes in next-generation zinc-based batteries: Toward practical energy storage systems. *J. Electroanal. Chem.*, 1001:119653, 2026.

[4] Benedetto Bozzini, Marco Boniardi, Tommaso Caielli, Andrea Casaroli, Elisa Emanuele, Lucia Mancini, Nicola Sodini, and Jacopo Strada. Electrochemical cycling behaviour and shape changes of Zn electrodes in mildly acidic aqueous electrolytes containing quaternary ammonium salts. *ChemElectroChem*, 10(12):e202201130, 2023.

[5] S. Kheawhom, R. Khezri, S. Motlagh, M. Etesami, A. A. Mohamad, F. Mahlendorf, and A. Somwangthanaroj. Stabilizing zinc anodes for different configurations of rechargeable zinc–air batteries. *Chem. Eng. J.*, 449:137796, 2022.

[6] Y. Sun, Y. Ou, Z. Cai, J. Wang, R. Zhan, S. Liu, and Z. Lu. Reversible aqueous Zn battery anode enabled by a stable complexation adsorbent interface. *EcoMat*, 4(4):e12167, 2022.

[7] Benedetto Bozzini, M. Kazemian, Francesca Rossi, Andrea Casaroli, Tommaso Caielli, B. Kaulich, M. Kiskinova, and Ivonne Sgura. X–ray imaging and micro–spectroscopy unravel the role of zincate and zinc oxide in the cycling of zinc anodes in mildly acidic aqueous electrolytes. *J. Power Sources*, 524:231063, 2022.

[8] Kevin N. Wood, E. Kazyak, A. F. Chadwick, K. H. Chen, J. G. Zhang, K. Thornton, and Neil P. Dasgupta. Dendrites and pits: untangling the complex behavior of lithium metal anodes through operando video microscopy. *ACS Cent. Sci.*, 2(11):790–801, 2016.

[9] Z. Wang, Z. Sun, J. Li, Y. Shi, C. Sun, B. An, H. M. Cheng, and F. Li. Insights into the deposition chemistry of Li ions in nonaqueous electrolyte for stable Li anodes. *Chem. Sci.*, 9(6):1506–1515, 2018.

[10] Ivonne Sgura, L. Mainetti, F. Negro, Maria Grazia Quarta, and Benedetto Bozzini. Deep-learning based parameter identification enables rationalization of battery material evolution in complex electrochemical systems. *Electrochim. Acta*, 404:139714, 2022.

[11] Maria Grazia Quarta, Ivonne Sgura, Elisa Emanuele, Jacopo Strada, Raquel Barreira, and Benedetto Bozzini. A deep-learning approach to parameter fitting for a lithium metal battery cycling model, validated with experimental cell cycling time series. *Sci. Rep.*, 15:4620, 2025.

[12] Maria Grazia Quarta, Ivonne Sgura, Massimo Frittelli, Raquel Barreira, and Benedetto Bozzini. Shape classification of battery cycling profiles via K-means clustering based on a Sobolev distance. *J. Comput. Appl. Math.*, 483:117365, 2026.

[13] K. Chayambuka, G. Mulder, D. L. Danilov, and P. H. L. Notten. Physics-based modeling of sodium-ion batteries part II. Model and validation. *Electrochim. Acta*, 404:139764, 2022.

[14] W. Fang, H. Chen, and F. Zhou. Fault diagnosis for cell voltage inconsistency of a battery pack in electric vehicles based on real-world driving data. *Comput. Electr. Eng.*, 102:108095, 2022.

[15] Y. Tian, S. Zhang, and Y. Wang. *Mathematical Modeling for Enhanced Electrochemical Properties*. CRC Press, Boca Raton, FL, USA, 1 edition, 2023.

[16] Alejandro A. Franco, Marie-Liesse Doublet, and Wolfgang G. Bessler. *Physical Multiscale Modeling and Numerical Simulation of Electrochemical Devices for Energy Conversion and Storage*. Springer, Cham, Switzerland, 2016.

[17] John Newman and Nitash P. Balsara. *Electrochemical Systems*. Wiley, Hoboken, NJ, USA, 4 edition, 2021.

[18] Á. G. Miranda and C. W. Hong. Integrated modeling for the cyclic behavior of high power Li-ion batteries under extended operating conditions. *Appl. Energy*, 111:681–689, 2013.

[19] Ivonne Sgura, A. S. Lawless, and Benedetto Bozzini. Parameter estimation for a morphochemical reaction-diffusion model of electrochemical pattern formation. *Inverse Probl. Sci. Eng.*, 26(5):618–647, 2018.

[20] K. H. Chen, K. N. Wood, E. Kazyak, W. S. LePage, A. L. Davis, A. J. Sanchez, and N. P. Dasgupta. Dead lithium: Mass transport effects on voltage, capacity, and failure of lithium metal anodes. *J. Mater. Chem. A*, 5(23):11671–11681, 2017.

[21] C. C. Li, W. Du, E. H. Ang, Y. Yang, Y. Zhang, and M. Ye. Challenges in the material and structural design of zinc anode towards high-performance aqueous zinc-ion batteries. *Energy Environ. Sci.*, 13:3910–3946, 2020.

[22] R. Shivkumar, G. Paruthimal Kalaignan, and T. Vasudevan. Effect of additives on zinc electrodes in alkaline battery systems. *J. Power Sources*, 55(1):53–62, 1995.

[23] Mukul Jain, Amanda L. Elmore, Michael A. Matthews, and John W. Weidner. Thermodynamic considerations of the reversible potential for the nickel electrode. *Electrochim. Acta*, 43(18):2649–2660, 1998.

[24] R. Barnard, C. F. Randell, and F. L. Tye. Studies concerning charged nickel hydroxide electrodes. II. Thermodynamic considerations of the reversible potentials. *J. Appl. Electrochem.*, 10(1):127–141, 1980.

[25] Benedetto Bozzini, D. Lacitignola, C. Mele, and Ivonne Sgura. Morphogenesis in metal electrodeposition. *Note Mat.*, 32:1–39, 2012.

[26] Benedetto Bozzini, D. Lacitignola, and Ivonne Sgura. Spatio-temporal organisation in alloy electrodeposition: a morphochemical mathematical model and its experimental validation. *J. Solid State Electrochem.*, 17:2605–2616, 2013.

[27] C. P. Chen and J. Jorne. Fractal analysis of zinc electrodeposition. *J. Electrochem. Soc.*, 137(9):2825–2832, 1990.

[28] S. Fletcher. Electrochemical deposition of hemispherical nuclei under diffusion control. some theoretical considerations. *J. Chem. Soc. Faraday Trans. 1*, 79:467–479, 1983.

[29] S. B. Lai, M. I. Jamesh, X. C. Wu, Y. L. Dong, J. H. Wang, and M. Gao. A promising energy storage system: Rechargeable Ni–Zn battery. *Rare Met.*, 36(5):381–396, 2017.

[30] H. Zhang, R. Wang, D. Lin, Y. Zeng, and X. Lu. Ni-based nanostructures as high-performance cathodes for rechargeable Ni–Zn battery. *ChemNanoMat*, 4(6):525–536, 2018.

[31] L. Li, S. Cheng, L. Deng, T. Liu, W. Dong, Y. Liu, and X. Wang. Effective solution toward the issues of Zn-based anodes for advanced alkaline Ni-Zn batteries. *ACS Appl. Mater. Interfaces*, 15(3):3953–3960, 2023.

[32] J. Li, T. Zhao, E. Shangguan, Y. Li, L. Li, and D. Wang. Enhancing the rate and cycling performance of spherical ZnO anode material for advanced zinc-nickel secondary batteries by combined in-situ doping and coating with carbon. *Electrochim. Acta*, 236:180–189, 2017.

[33] W. Long, Z. Yang, X. Fan, B. Yang, Z. Zhao, and J. Jing. The effects of carbon coating on the electrochemical performances of ZnO in Ni-Zn secondary batteries. *Electrochim. Acta*, 105:40–46, 2013.

[34] L. Zhao, S. Lei, Q. Tu, L. Rao, W. Zen, Y. Xiao, and B. Cheng. Phase-controlled growth of nickel hydroxide nanostructures on nickel foam for enhanced supercapacitor performance. *J. Energy Storage*, 43:103171, 2021.

[35] X. R. Yi, H. P. Sun, N. Robertson, and C. Kirk. Nanoflower $Ni(OH)_2$ grown in situ on Ni foam for high-performance supercapacitor electrode materials. *Sustain. Energy Fuels*, 5(19):5236–5246, 2021.

[36] Z. Zhang, H. Huo, Z. Yu, L. Xiang, B. Xie, C. Du, J. Wang, and G. Yin. Unraveling the reaction mechanism of low dose Mn dopant in $Ni(OH)_2$ supercapacitor electrode. *J. Energy Chem.*, 61:497–506, 2021.

[37] J. Hao, L. Yan, X. Zou, Y. Bai, Y. Han, C. Zhu, Y. Zhou, and B. Xiang. Series of halogen engineered $Ni(OH)_2$ nanosheet for pseudocapacitive energy storage with high energy density. *Small*, 19(34):2300467, 2023.

[38] S. Verma, S. Arya, V. Gupta, S. Mahajan, H. Furukawa, and A. Khosla. Performance analysis, challenges and future perspectives of nickel based nanostructured electrodes for electrochemical supercapacitors. *J. Mater. Res. Technol.*, 11:564–599, 2021.

[39] M. Zhou, X. Zhou, Y. Yang, H. Yin, Y. Lei, and S. Liang. Issues and optimization strategies of binders for aqueous zinc metal batteries. *Chem. Eng. J.*, 497:154432, 2024.

[40] D. Stock, S. Dongmo, J. Janek, and D. Schröder. Benchmarking anode concepts: the future of electrically rechargeable zinc-air batteries. *ACS Energy Lett.*, 4(6):1287–1300, 2019.

[41] Z. Feng, Z. Yang, J. Huang, X. Xie, and Z. Zhang. The superior cycling performance of the hydrothermal synthesized carbon-coated ZnO as anode material for zinc-nickel secondary cells. *J. Power Sources*, 276:162–169, 2015.

[42] Y. Zhang, E. Ang, Y. Yang, M. Ye, W. Du, and C. Li. Interlayer chemistry of layered electrode materials in energy storage devices. *Adv. Funct. Mater.*, 31(12):2007358, 2021.

[43] F. Gu, X. Cheng, S. Wang, X. Wang, and P. S. Lee. Oxidative intercalation for monometallic Ni^{2+}–Ni^{3+} layered double hydroxide and enhanced capacitance in exfoliated nanosheets. *Small*, 11(17):2044–2050, 2015.

[44] B. Liu, X. Liu, X. Fan, J. Ding, W. Hu, and C. Zhong. 120 years of nickel-based cathodes for alkaline batteries. *J. Alloys Compd.*, 834:155185, 2020.

[45] M. Jiang, D. L. Danilov, R. A. Eichel, and P. H. L. Notten. A review of degradation mechanisms and recent achievements for Ni-rich cathode-based Li-ion batteries. *Adv. Energy Mater.*, 12(6):2103005, 2022.

[46] Joel H. Hildebrand. *The Solubility of Nonelectrolytes*. Reinhold Publishing, New York, NY, USA, 1950.

[47] Edward A. Guggenheim. *Mixtures*. Oxford University Press, Oxford, UK, 1952.

[48] O. Tillement and M. Quarton. Thermodynamic model of intercalation electrodes. *J. Electrochem. Soc.*, 140(7):1870–1878, 1993.

[49] S. Atlung. The chemical potential of the proton-electron pair. *J. Electroanal. Chem. Interfacial Electrochem.*, 79(1):1–18, 1977.

[50] B. Sambandam, V. Mathew, F. A. Nurul, S. Kim, M. Song, and J. Kim. Aqueous rechargeable zinc–metal batteries: A critical analysis. *ACS Energy Lett.*, 9:3058–3065, 2024.

[51] A. Latz and J. Zausch. Thermodynamic derivation of a butler–volmer model for intercalation in Li-ion batteries. *Electrochim. Acta*, 110:358–362, 2013.

[52] Y. Liu, J. Li, Y. Liu, M. Wang, K. Liu, and H. Cui. Revealing the key factors determining its electrochemical performance and hereby establishing a carbon shell-protected structure as high-performance electrode material for supercapacitors. *J. Energy Storage*, 81:110436, 2024.

[53] S. C. Wu, M. C. Tsai, H. J. Liao, T. Y. Su, S. Y. Tang, and C. W. Chen. Intercalation of zinc monochloride cations by deep eutectic solvents for high-performance rechargeable non-aqueous zinc ion batteries. *Chem. Eng. J.*, 433:133516, 2022.

[54] Ivonne Sgura and Benedetto Bozzini. Numerical issues related to the modelling of electrochemical impedance data by non-linear least-squares. *Int. J. Non-Linear Mech.*, 40:557–570, 2005.

[55] X. Lu, H. J. Chang, J. F. Bonnett, N. L. Canfield, K. Jung, V. L. Sprenkle, and G. Li. Effect of cathode thickness on the performance of planar Na-$NiCl_2$ battery. *J. Power Sources*, 243:1033–1039, 2013.

[56] H. Wang, P. Zhang, K. Wang, Y. Zuo, M. Wei, Z. Chen, N. Shang, and P. Pei. A self–designed double cross–linked gel for flexible zinc–air battery with extreme conditions adaptability. *Chem. Eng. J.*, 451:138622, 2023.

[57] I. W. Seong, C. H. Hong, B. K. Kim, and W. Y. Yoon. The effects of current density and amount of discharge on dendrite formation in the lithium powder anode electrode. *J. Power Sources*, 178(2):769–773, 2008.

[58] Z. Wang, Z. Sun, J. Li, Y. Shi, C. Sun, B. An, H. M. Cheng, and F. Li. Insights into the deposition chemistry of Li ions in nonaqueous electrolyte for stable Li anodes. *Chem. Soc. Rev.*, 50(5):3178–3210, 2021.

[59] W. Chen, X. Zheng, and T. Ahmad. Challenges and strategies on Zn electrodeposition for stable Zn-ion batteries. *Energy Storage Mater.*, 39:59–76, 2021.

A. Details of the Fitted Curve

A.1. Equilibrium curve

The equilibrium curve cannot be obtained experimentally, since it is not possible to perform measurements at zero current. For this reason, the quasi-equilibrium curve during charge and discharge, obtained at a C-rate equal to C/50, was adopted as the reference curve. At such a low current rate, dynamic effects are strongly reduced, and the measured voltage provides a satisfactory approximation of the system equilibrium voltage. The experimental data used in this work are taken from Amin's thesis

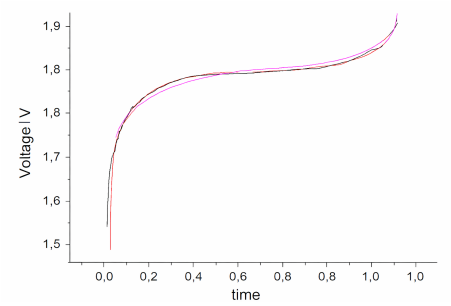

Figure 18: 'equilibrium discharge curve'

In red, the cubic fit is shown, while in purple the quadratic model is represented. From the image, it is possible to see how the cubic fit is able to capture the asymmetries of the discharge curve.

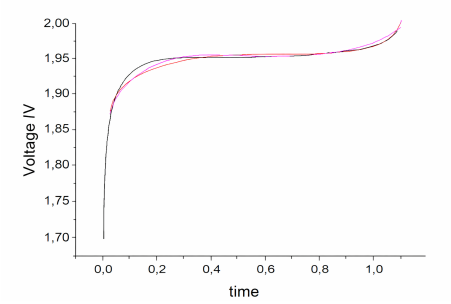

Figure 19: 'equilibrium charge curve'

As before, also in the charging curve, the cubic model fit (shown in red) is able to better follow the shape, although the improvement is less evident.

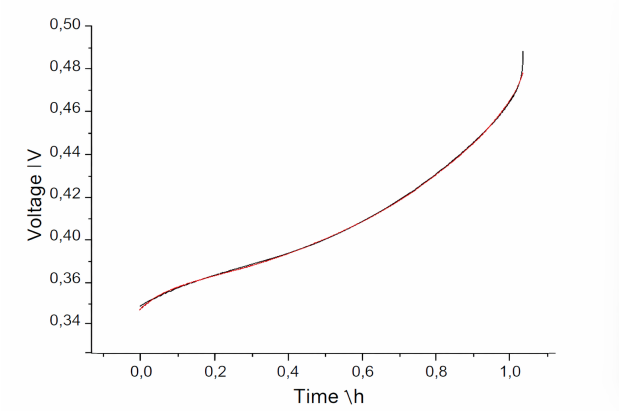

$0.6\,\mathrm{mA\,cm^{-2}}$

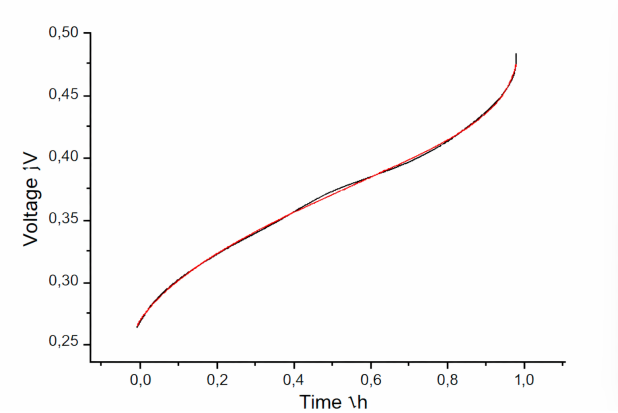

$0.75\,\mathrm{mA\,cm^{-2}}$

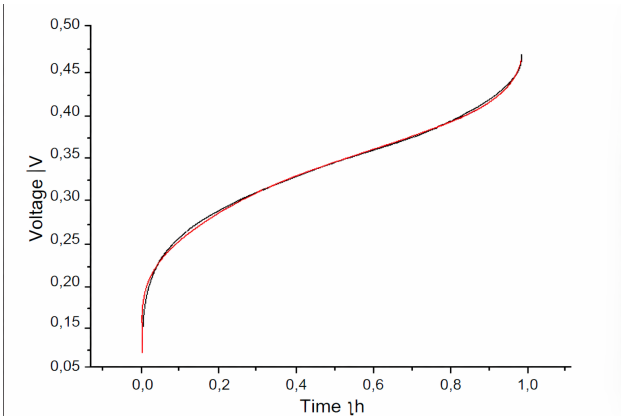

$1.2\,\mathrm{mA\,cm^{-2}}$

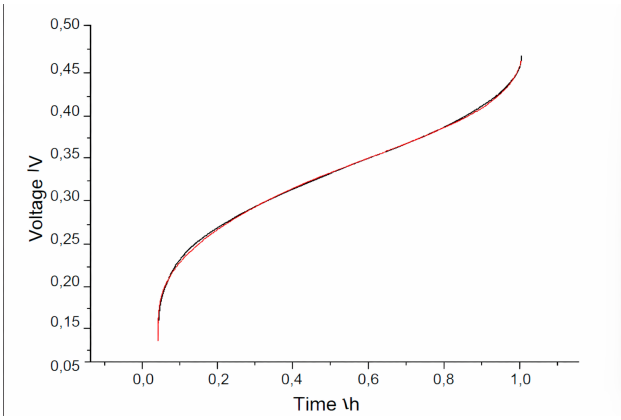

$3\,\mathrm{mA\,cm^{-2}}$

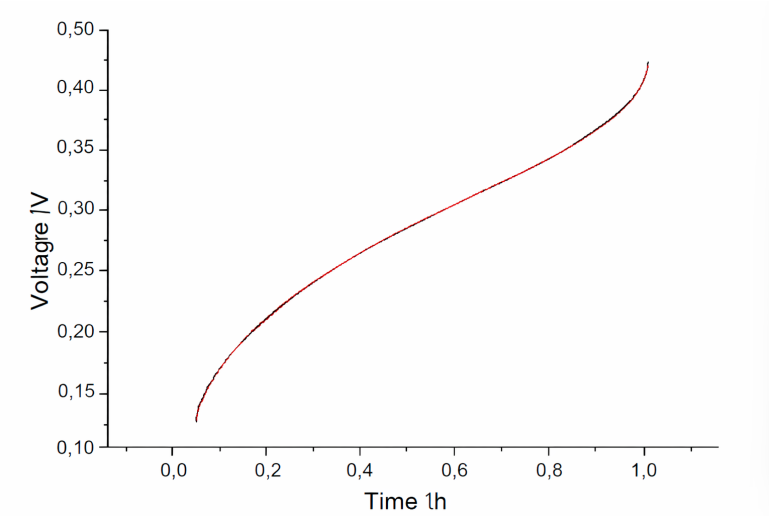

$6\,\mathrm{mA\,cm^{-2}}$

Figure 20: Fit of discharge curves at different current densities.

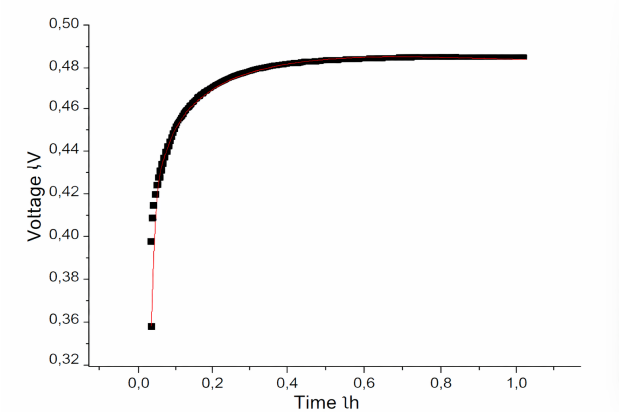

$0.3\,\mathrm{mA\,cm^{-2}}$

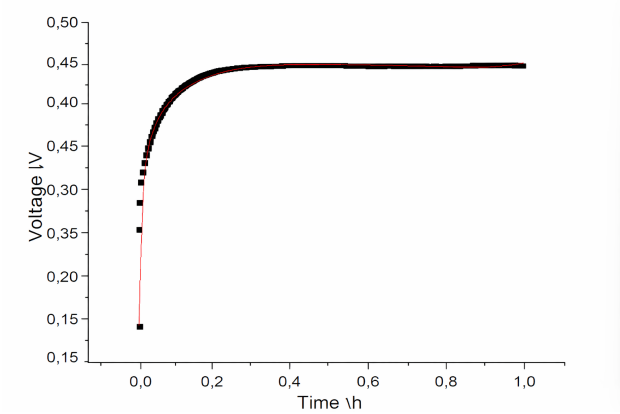

$0.6\,\mathrm{mA\,cm^{-2}}$

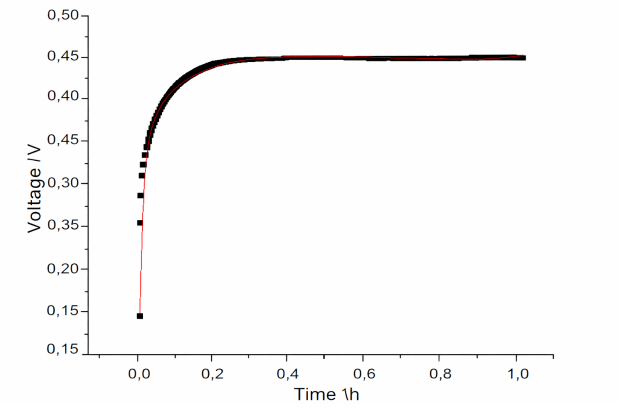

$1.5\,\mathrm{mA\,cm^{-2}}$

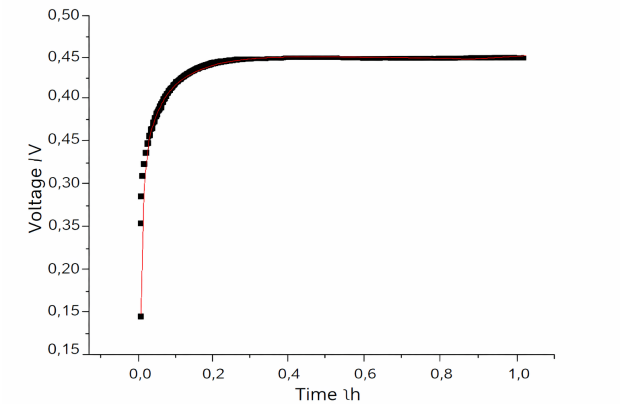

$3\,\mathrm{mA\,cm^{-2}}$

Figure 21: Fit of charge curves at different current densities.

A.2. fitting of parameters A, B and E0

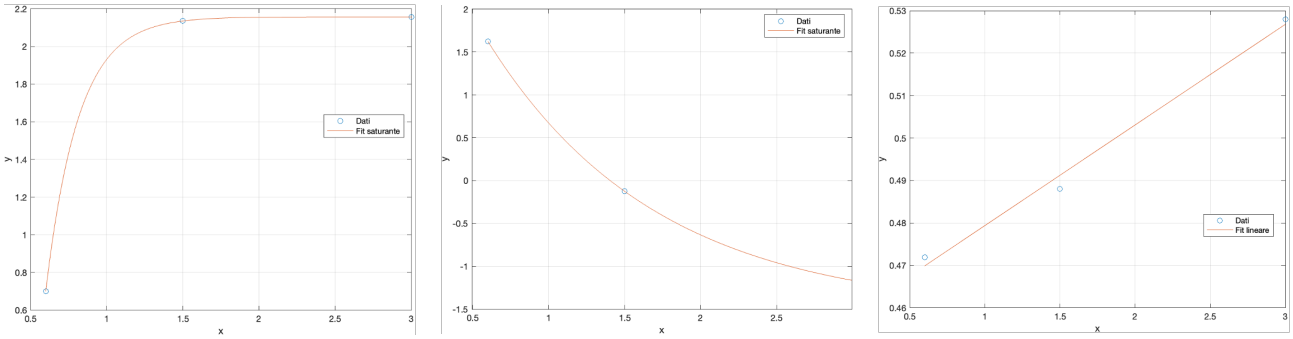

(A) (B) (E0)

Figure 22: Fitting of Parameters A, B, and E_0 for the charge curves.

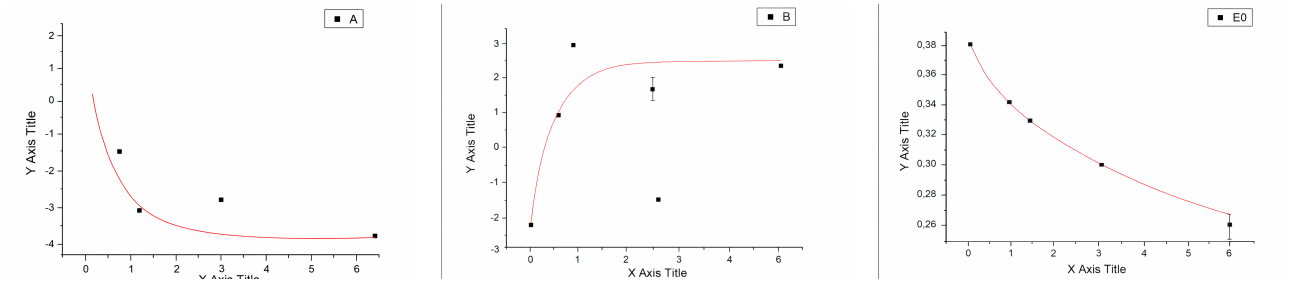

(A) (B) (E0)

Figure 23: Fitting of Parameters A, B, and E_0 for the discharge curves.

A.3. Additional Material for Shape Recognition of symmetric cell

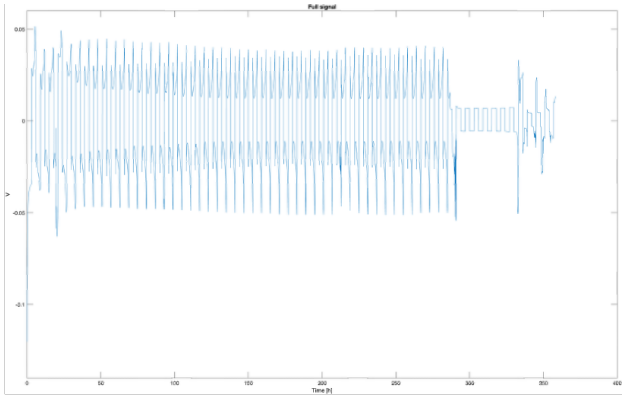

(NSBD195)

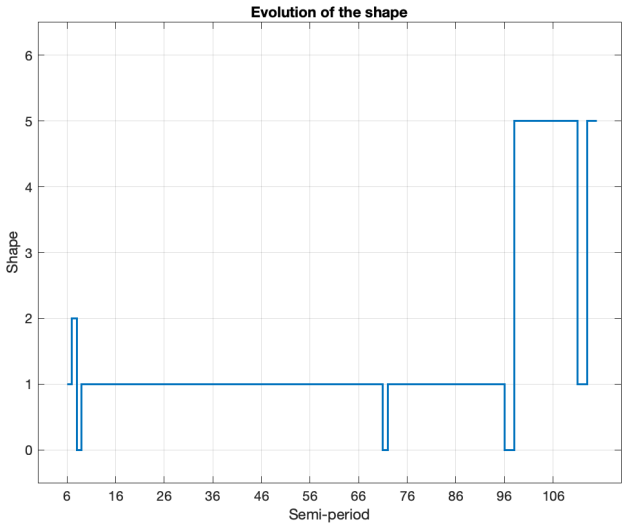

(NSBD195)

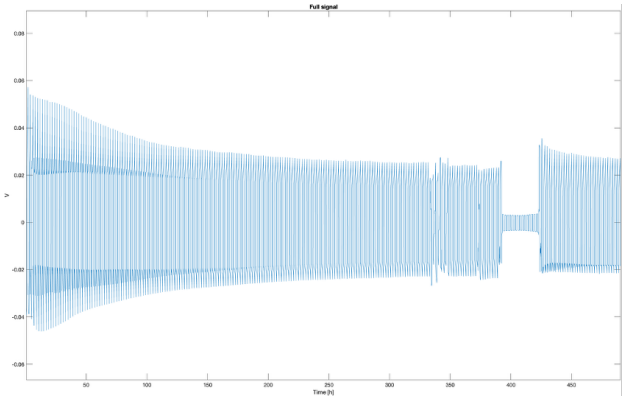

(NSBD201)

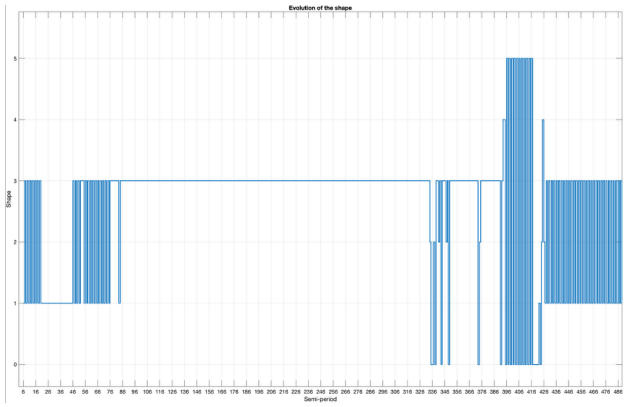

(NSBD201)

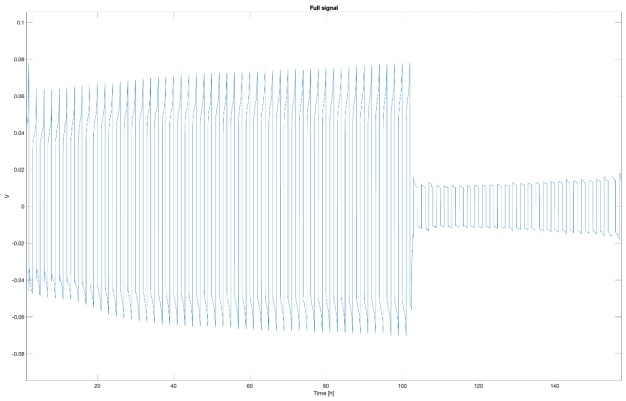

(NSBD257)

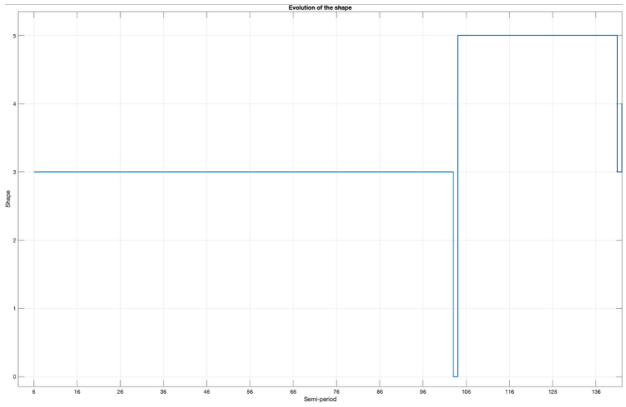

(NSBD257)

Figure 24: Zwitterions cells.

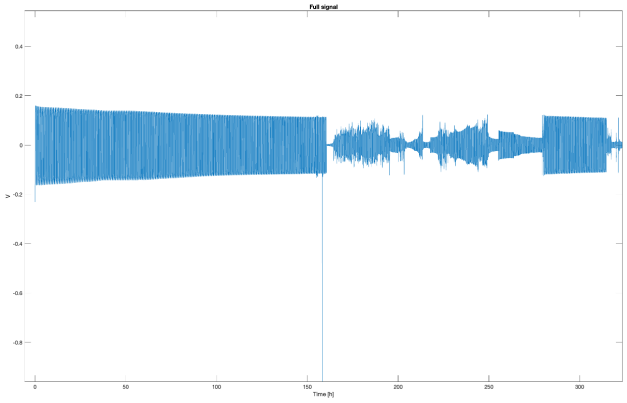

(punched)

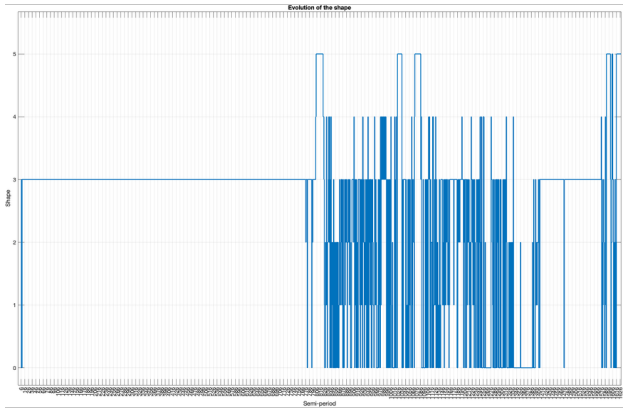

(punched)

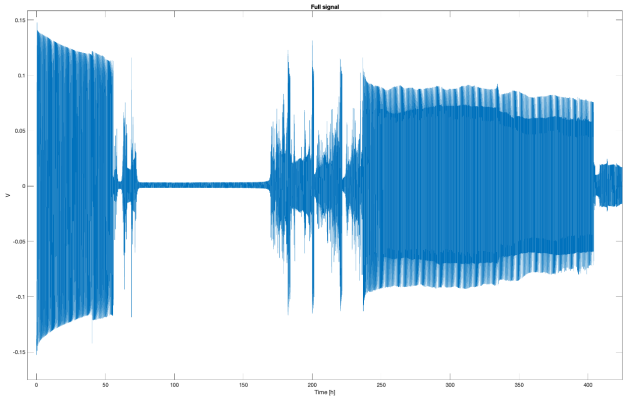

(Shielded punched)

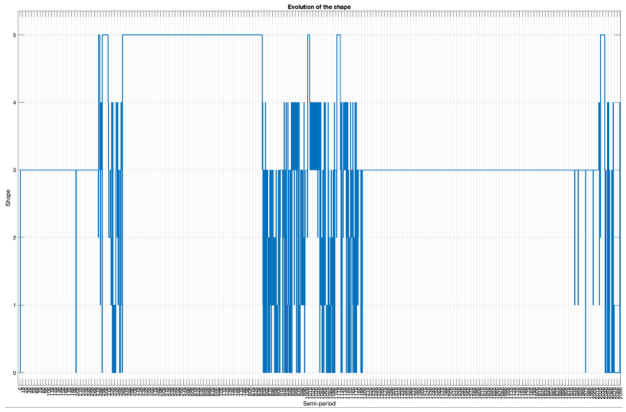

(Shielded punched)

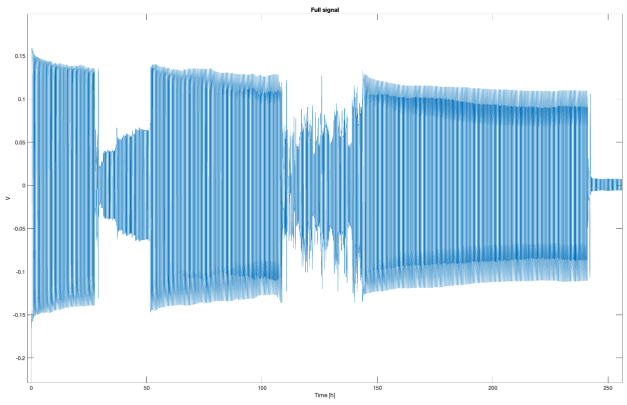

(laser cut)

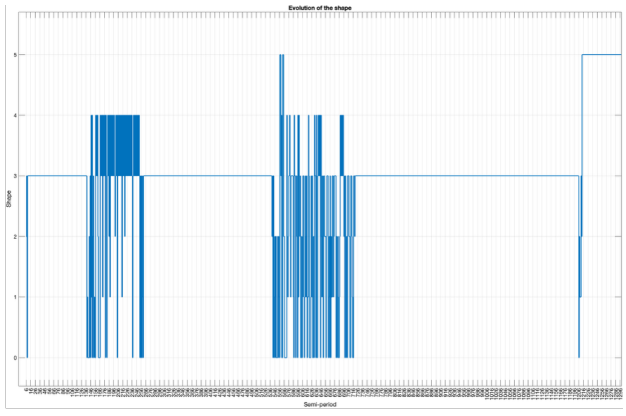

(laser cut)

Figure 25: different cuts cell

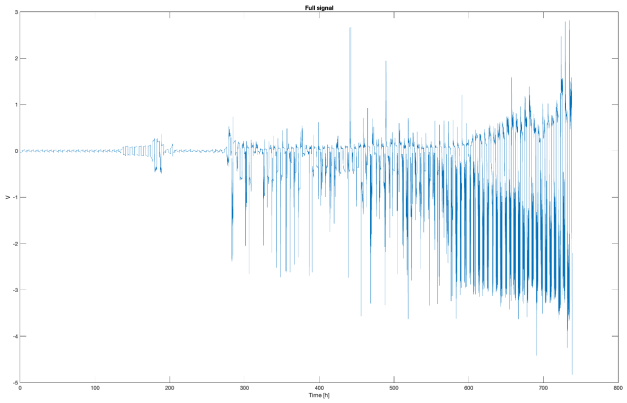

(AQ)

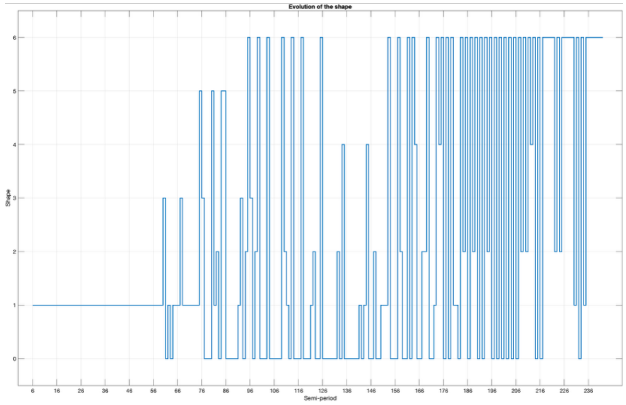

(AQ)

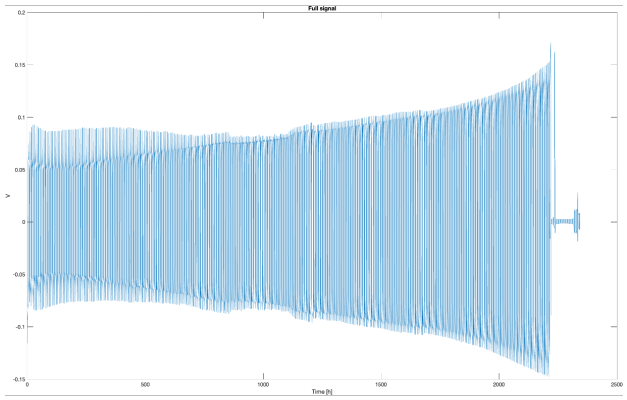

($ZnSO_4EG$)

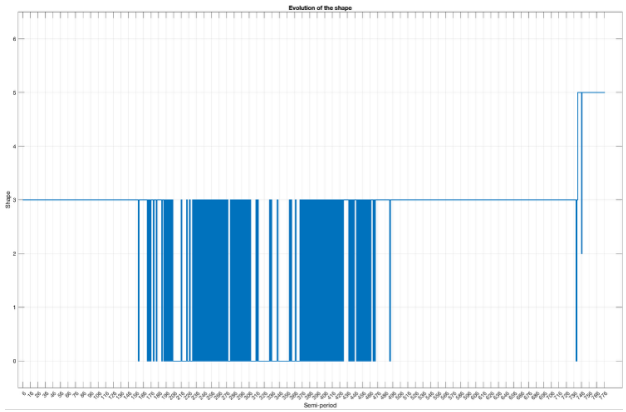

($ZnSO_4EG$)

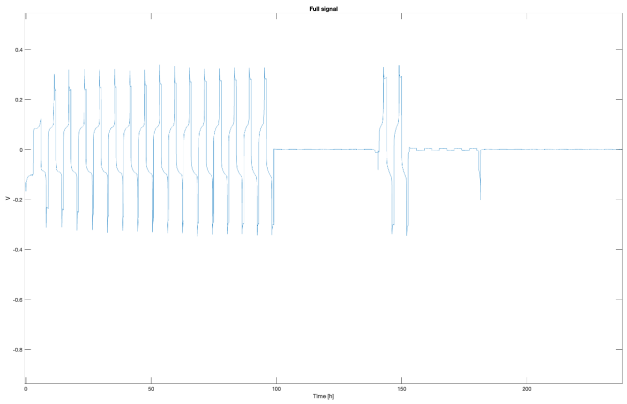

(DESEG50%)

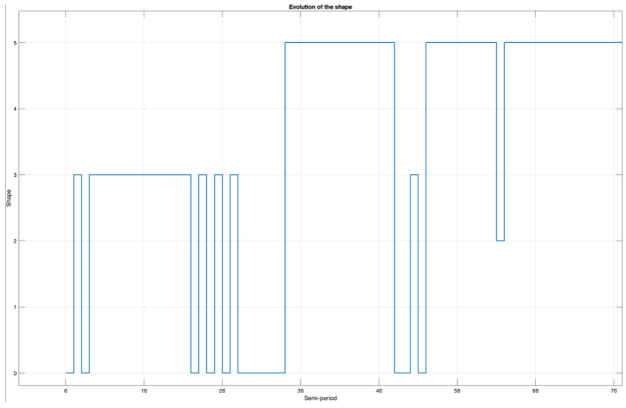

(DESEG50%)

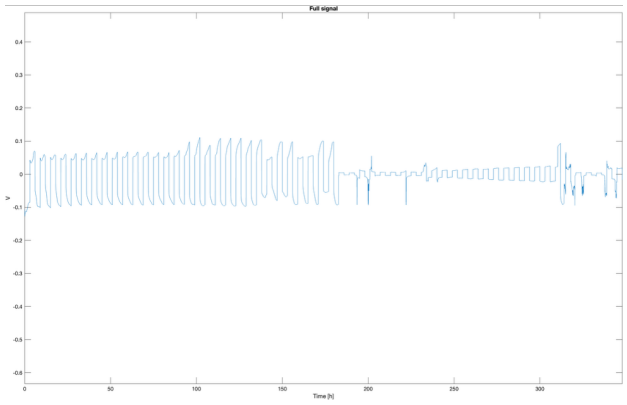

(TBAB)

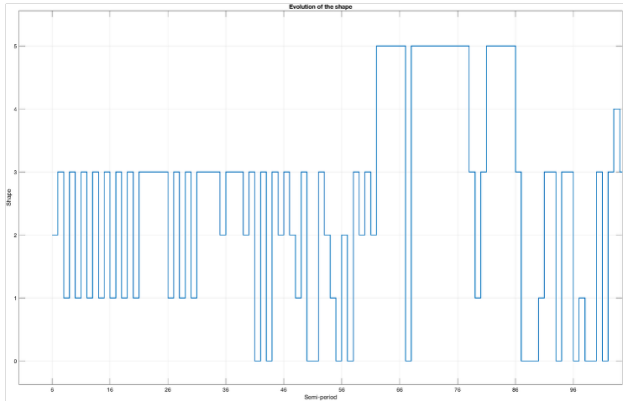

(TBAB)

Figure 26: DES and aqueous electrolyte of symmetric cells

A.4. Additional Material for Shape Recognition of full cell

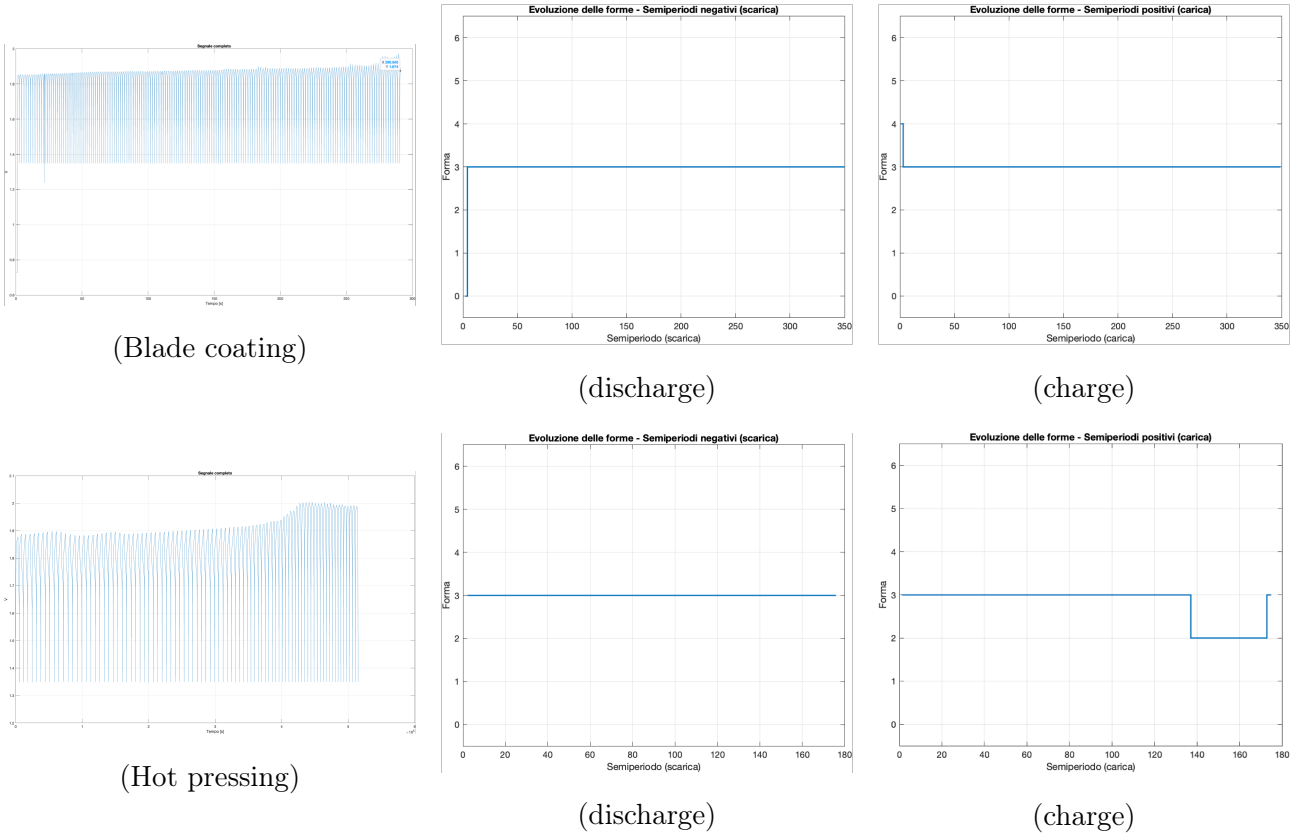

(Blade coating) (discharge) (charge)

(Hot pressing) (discharge) (charge)

Figure 27: Blade coating Vs Hot pressing.

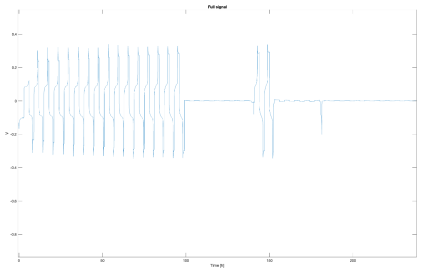

(ZnSO4 DESEG 2M)

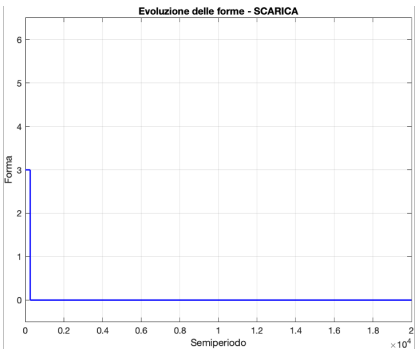

(discharge)

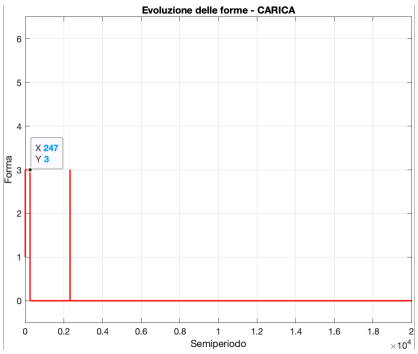

(charge)

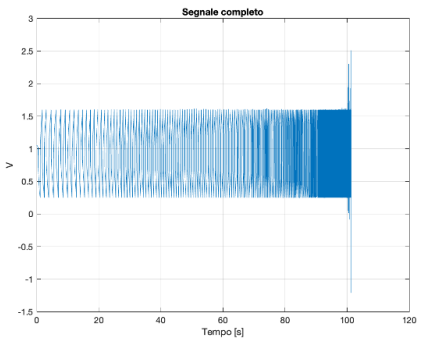

(DESEG 50)

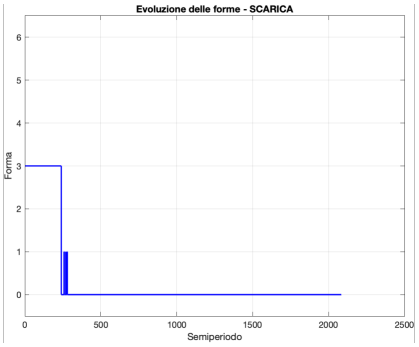

(discharge)

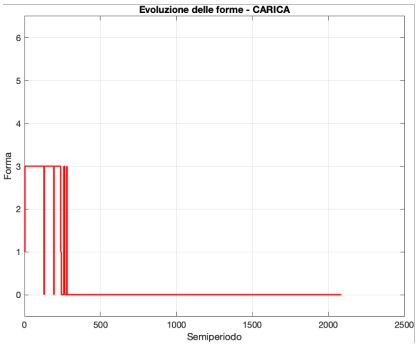

(charge)

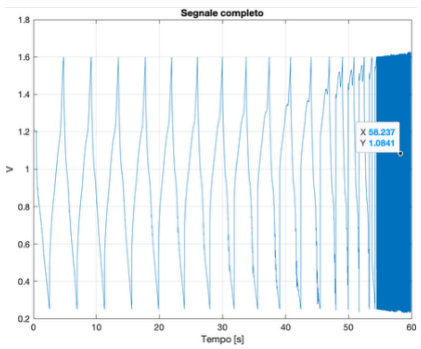

(DESEG+TBAB)

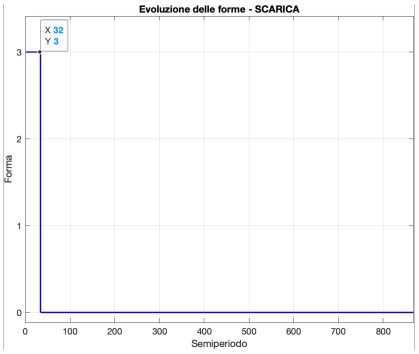

(discharge)

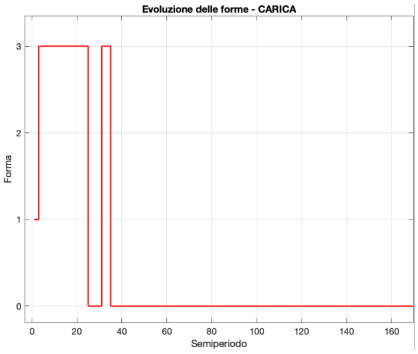

(charge)

Figure 28: DES electrolyte full cells

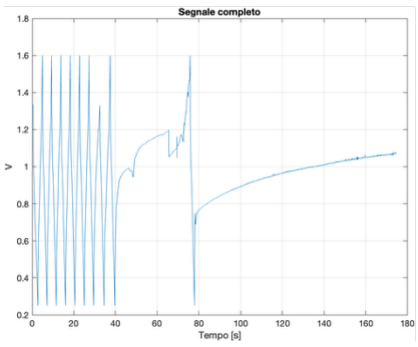

(Split cell CMC + TQC cathode)

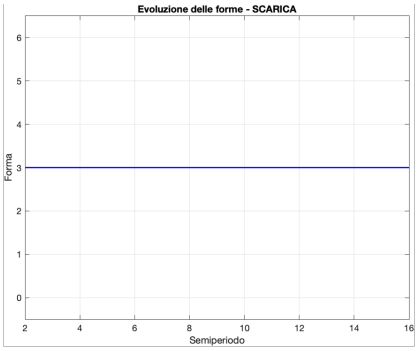

(discharge)

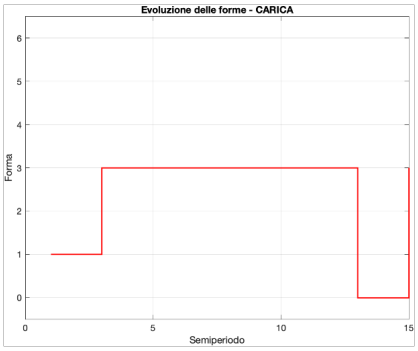

(charge)

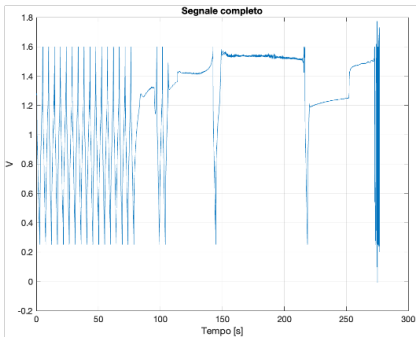

(split cell)

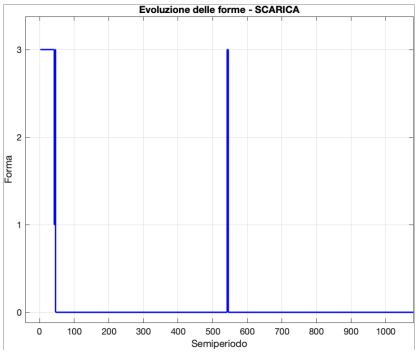

(discharge)

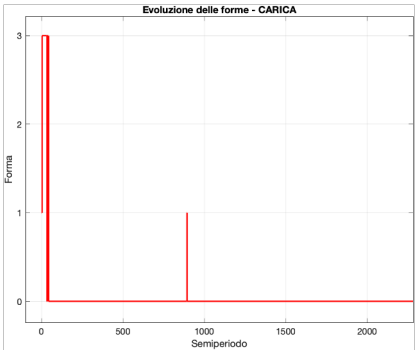

(charge)

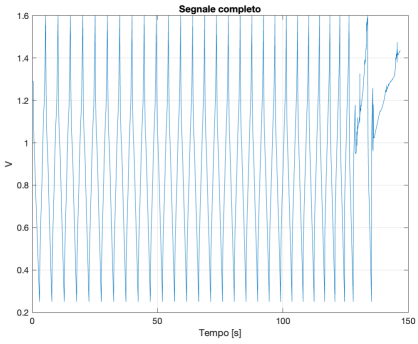

(TQC cathode)

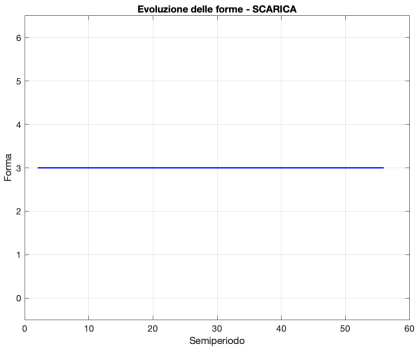

(discharge)

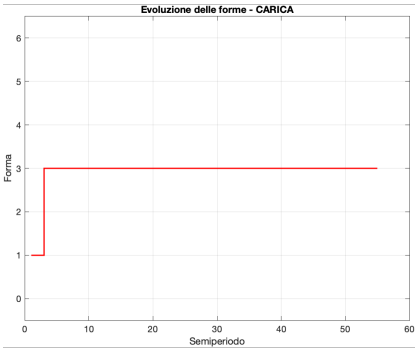

(charge)

Figure 29: CMC and TQC cathode

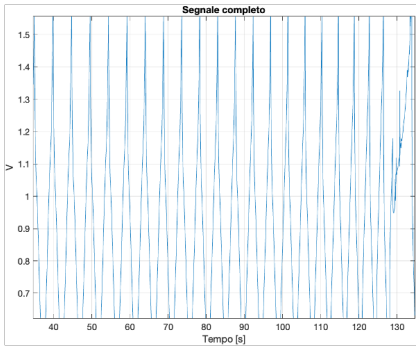

(swadgelock cell TQC cathode)

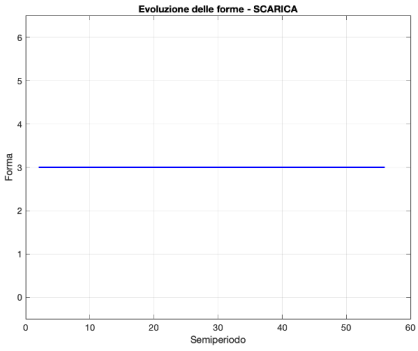

(swadgelock cell TQC cathode)

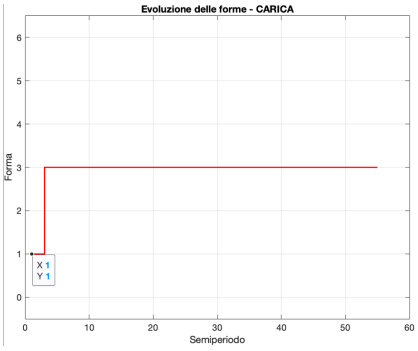

(swadgelock cell TQC cathode)

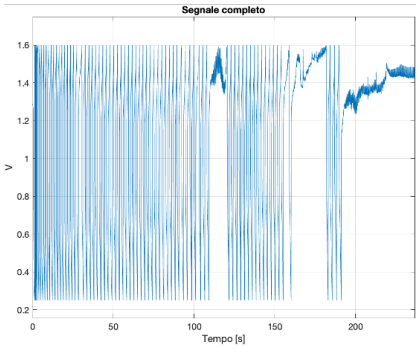

(Svit cell)

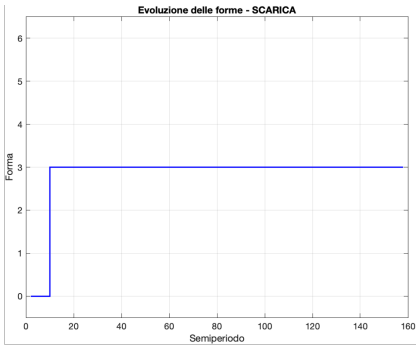

(Svit cell)

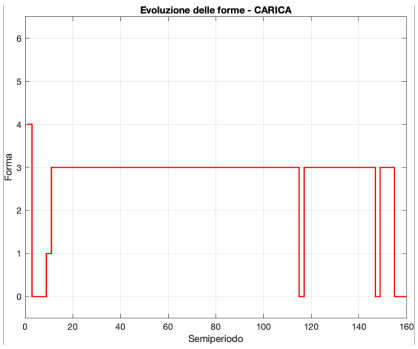

(Svit cell)

Figure 30: Additional data.

B. Additional Material for sensitivity analysis

It is interesting to note that if the order of perturbation is increased from one order to two orders of magnitude, by increasing $k_{0,\text{fast}}$ or decreasing $k_{0,\text{slow}}$ (both producing the same effect),shape 3 reverses and becomes monotonically decreasing, namely shape 4. This could indicate that when Morphology 4 is observed, the system is dominated by high values of $k_{0,\text{fast}}$.: high values of $k_{0,\text{fast}}$ indicate that the electrochemical reaction is extremely rapid at the tips of the protrusions. Physically, this is due to a strong intensification of the electric field at the apex of the dendrites, caused by their reduced radius of curvature. As a consequence, an increase in the local current density at the tip (j_{tip}) occurs compared to the flat regions of the electrode.
Since $k_{0,\text{fast}}$ quantifies the reaction rate in the most reactive regions, high values indicate accelerated interfacial growth dynamics. In other words, the metal tends to deposit preferentially on existing protrusions rather than uniformly, thereby promoting faster and uncontrolled dendritic growth. This interpretation is fully consistent with experimental observations: Morphology 4 is observed almost exclusively during cell restart following short-circuit failure. Under these conditions, the electrode surface exhibits pronounced roughness, leading to strong electric field localization at protrusion tips. Consequently, interfacial kinetics dominate over mass transport effects, and the system response becomes governed by highly localized reaction rates. This results in the characteristic monotonically decreasing voltage profile associated with shape 4.

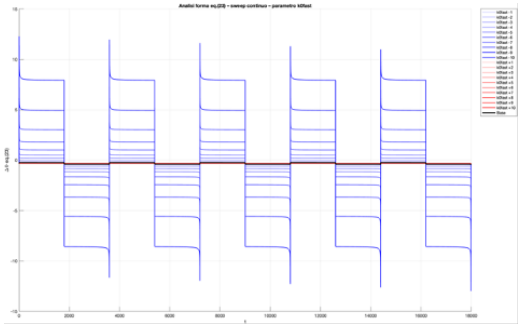

Figure 31: Effects of smaller small $k_{0,\text{slow}}$

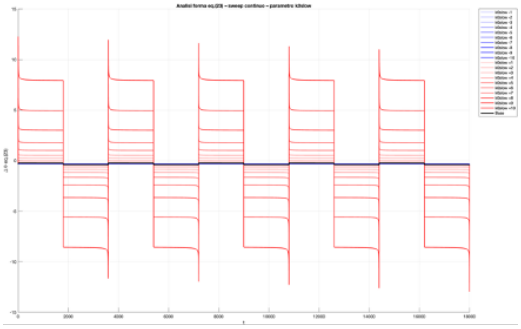

Figure 32: Effect of higher $k_{0,\text{fast}}$

B.1. $k_{0,\text{slow}}$ plot

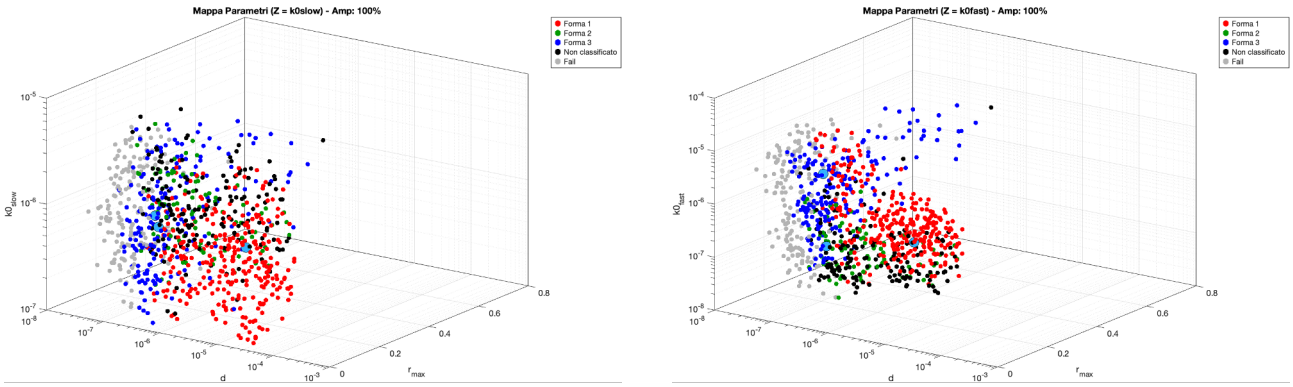

Figure 33: $k_{0,\text{fast}}$ Vs $k_{0,\text{slow}}$ plot

As in the previous case, each point in the mapping corresponds to a variation of all four parameters. However, in this representation the dependence on the parameter $k_{0,\text{slow}}$ is made explicit. As can be observed, this parameter also exerts an influence on the morphology of the transients. Nevertheless, the overall distribution of waveform families remains unchanged. The only noticeable difference is that the points appear more compressed, since the variation along the z-axis (associated with $k_{0,\text{slow}}$) is now smaller.
This suggests that, although both $k_{0,\text{slow}}$ and $k_{0,\text{fast}}$ have a certain impact on the transient shapes, their influence remains weaker compared to that of the parameters r and d.

C. Waveform Classification Algorithm

Listing 1: Derivative-sign-based waveform classification algorithm

```
s = sign(mean_der(kk,:));

if (s(1)>0  && s(5)<0 && s(6)<0) || ...
   (s(1)<0 && s(2)>0 && s(3)>0 && s(6)<0)
    category(kk) = "shape 2";

elseif (s(1)<0 && s(5)>0 && s(6)>0) || ...
       (s(2)<0 && s(5)>0 && s(6)>0)
    category(kk) = "shape 1";

elseif s(2)>0 && s(3)>0 && s(4)>0 && s(5)>0 && s(6)>0
    category(kk) = "shape 3";

elseif s(2)<0 && s(3)<0 && s(4)<0 && s(5)<0
    category(kk) = "shape 4";

else
    category(kk) = "unclassified";
end
```

Abstract in lingua italiana

Il cycling galvanostatico di celle metalliche simmetriche rappresenta una piattaforma fondamentale per l'investigazione delle instabilità morfologiche nelle batterie ad alta densità energetica. Tuttavia, l'analisi convenzionale delle celle simmetriche Zn/Zn si basa tipicamente su descrittori integrali, quali il tempo al guasto, trascurando la ricca informazione fisico-chimica contenuta nei transitori di tensione.
Il presente lavoro introduce un quadro teorico basato sulla fisica che combina il modello Metal Anode Charging (MAC) con una classificazione automatizzata delle forme d'onda. I transitori di tensione vengono rigorosamente suddivisi in quattro famiglie morfologiche caratteristiche, sulla base delle proprietà di curvatura e delle firme derivate, ciascuna associata a distinti regimi di trasporto ionico, cinetica elettrochimica, crescita dendritica e passivazione.
Un algoritmo di riconoscimento implementato in MATLAB consente un'analisi ad alto rendimento di dataset sperimentali, evidenziando come additivi e metodi di fabbricazione degli elettrodi modulino l'evoluzione morfologica e i meccanismi di degradazione.
Il quadro metodologico viene ulteriormente esteso dalle celle simmetriche Zn/Zn a una configurazione completa Ni/Zn, mediante l'integrazione di una descrizione termodinamicamente consistente del catodo Ni/NiOOH basata sul formalismo di Margules a due parametri. Tale transizione trasforma il sistema da un problema simmetrico dominato dal trasporto a un modello ibrido asimmetrico che accoppia la crescita dello zinco controllata dalla morfologia con la termodinamica di intercalazione allo stato solido.
I risultati dimostrano che la morfologia delle forme d'onda di tensione costituisce un descrittore diagnostico robusto, in grado di collegare le firme elettrochimiche ai regimi fisici sottostanti. Spostando l'attenzione dall'adattamento parametrico a un'interpretazione basata sulla morfologia, questo approccio definisce una metodologia generalizzabile per un monitoraggio fisicamente fondato dei sistemi di accumulo energetico a base di zinco.

Parole chiave: batterie zinco–zinco, celle Ni–Zn, modello MAC, classificazione dei transitori di tensione, modello di Margules, crescita dendritica, passivazione

Acknowledgements

I would like to express my deepest gratitude to my supervisor, Benedetto Bozzini, for his immense availability, constant support, and outstanding professionalism throughout the course of this work. His guidance has been invaluable, not only from a scientific perspective but also on a personal level.
Beyond his expertise and rigor, he has transmitted to me a genuine passion for scientific research, inspiring curiosity, critical thinking, and intellectual dedication. His enthusiasm for discovery and commitment to excellence have profoundly influenced my academic growth, and for this I am sincerely grateful.
I also thank the research group members for their support, collaboration, and valuable technical assistance during both the experimental and modeling phases of the project.
Finally, I am deeply grateful to my family and friends for their constant encouragement and support during this academic journey.